This manuscript has been submitted for publication in *JGR: Solid Earth*. Please note that this article has not been peer-reviewed before and is currently undergoing peer review for the first time. Subsequent versions of this manuscript may have slightly different content.

Effects of loading schemes in volumetric simulations of sequences of earthquakes and aseismic slip (SEAS) in subduction zones

Jeena Yun[1], Yuri Fialko[1], Dave A. May[1], Alice-Agnes Gabriel[1,2], Charles A. Williams[3], and Dunyu Liu[4]

[1]Scripps Institution of Oceanography, University of California San Diego, La Jolla, CA, USA
[2]Department of Earth and Environmental Sciences, Ludwig-Maximilians Universität München, Munich, Germany
[3]Earth Sciences New Zealand, Lower Hutt, New Zealand
[4]Institute for Geophysics, Jackson School of Geosciences, The University of Texas at Austin, TX, USA

Key Points:

- We systematically explore the effects of three loading schemes on modeled on- and off-fault deformation patterns in a 2D curved megathrust.
- Parallel and side push loading schemes result in a long-term accumulation of vertical displacements and fault-normal stresses.
- Subducting slab loading scheme reduces artifacts in multi-cycle simulations and gives rise to more realistic deformation patterns.

Corresponding author: Jeena Yun, j4yun@ucsd.edu

Abstract

State-of-the-art simulations of sequences of earthquakes and aseismic slip (SEAS) require realistic loading conditions and physics-based constitutive laws to produce the full spectrum of fault slip. Previous studies have shown that loading schemes may affect long-term system behavior, including earthquake recurrence intervals. However, the effects of loading schemes on rupture characteristics and off-fault deformation patterns remain poorly understood, particularly for non-planar dipping faults. Here, we systematically compare three loading schemes for a curved megathrust. In "parallel loading", we prescribe far-field velocities on the sides of a parallelogram-shaped domain aligned with the deep fault root. In "side push loading", we prescribe horizontal shortening. In "subducting slab loading", we prescribe a constant velocity at the bottom of the subducting plate. We find that earthquake sequences are similar under parallel and side push loading schemes, whereas additional complexity emerges under subducting slab loading, exhibiting different recurrence intervals, average slip, and stress drops. Parallel and side push loading schemes result in a long-term accumulation of vertical displacements and fault-normal stresses, which is mitigated under subducting slab loading. Among the three loading methods, subducting slab loading scheme produces deformation patterns most consistent with geodetic observations, including surface displacements due to earthquakes, afterslip, and slow slip events. We further examine the effects of domain length, slab thickness, and material heterogeneities on simulated rupture characteristics and deformation patterns. These results highlight the role of loading conditions on modeled deformation patterns in SEAS simulations.

Plain Language Summary

Simulations of sequences of earthquakes and aseismic slip (SEAS) are computer models that represent both fast earthquakes and slow fault motion, helping us understand how faults slip over many earthquake cycles. In these models, an important choice is how tectonic loading is applied at the model boundaries, which can affect earthquake recurrence. We compare three ways of loading a curved thrust fault, similar to faults in subduction zones where one tectonic plate dives beneath another. We find that two of the three loading methods introduce artificial stresses on the fault and produce long-term surface motion that grows over time, in contrast to geodetic observations. The third method, which represents pulling motion applied along a subducting slab, reduces both on-fault stresses and long-term surface motion by up to two orders of magnitude. Surface motions produced by this method also capture slow fault slip, consistent with that observed during natural earthquake cycles. Our results show that boundary conditions can strongly affect modeled deformation patterns, even with the same fault geometry and frictional properties. These results emphasize the need to carefully select loading conditions when using SEAS models to study subduction zone hazards.

1 Introduction

Subduction zones host the largest and most damaging earthquakes on Earth (e.g., Kato et al., 2012; Stein & Okal, 2005), and considerable effort is devoted to understanding the physics underlying megathrust earthquakes and mitigating the associated hazards. Unfortunately, observations of the earthquake cycle in subduction zones remain limited due to the scarcity of seafloor instrumentation (Govers et al., 2018; Hill et al., 2012; Lindsey et al., 2021; Yokota et al., 2018). Physics-based numerical simulations have emerged as valuable tools to overcome the limited spatiotemporal coverage of observations and to provide insights into subduction zone dynamics. For example, dynamic rupture simulations (Day, 1982; Harris & Day, 1999; Ramos et al., 2022), which focus on earthquake rupture and wave propagation during individual events, reveal the role of complex fault geometry (e.g., Ando & Kaneko, 2018; Kozdon et al., 2013), strength and stress

heterogeneities (e.g., Duan, 2012; Glehman et al., 2025; Weng & Yang, 2018; Wong et al., 2026), and off-fault plasticity (e.g., Ma & Hirakawa, 2013; Ulrich et al., 2019) for megathrust earthquake complexity.

Simulation of sequences of earthquakes and aseismic slip (SEAS; Erickson et al., 2020) is another physics-based modeling framework that aims to bridge all stages of seismic cycles from interseismic loading to coseismic rupture nucleation, propagation, and termination, spanning a wide range of time scales from millennia to milliseconds (Barbot et al., 2012; Lapusta et al., 2000; Rice, 1993). These simulations couple the elastodynamic equations to the experimentally inferred rate-and-state friction law (Dieterich, 1979; Ruina, 1983) to produce spontaneous evolutions of the slip history given fault geometries, elastic properties, and frictional properties.

Recent advances in computational resources and optimization methods allowed SEAS simulations to account for complex fault geometry (e.g., Biemiller et al., 2024; Ozawa & Ando, 2021; Romanet et al., 2018; Rodriguez Piceda et al., 2026; Tal & Gabrieli, 2024) or heterogeneous stress and strength conditions (e.g., Hillers et al., 2006; Jiang & Lapusta, 2016; Molina-Ormazabal et al., 2023). These realistic SEAS simulations have revealed the importance of variations in fault geometry, tectonic loading, and frictional properties in reproducing subduction zone earthquakes (e.g., Herrera et al., 2024; D. Li & Liu, 2016; Perez-Silva et al., 2022; Yu et al., 2018) and the interaction between seismic and aseismic processes (e.g., D. Li & Gabriel, 2024; Meng & Duan, 2023; Shibazaki et al., 2019).

In particular, SEAS simulation codes that utilize volume discretization provide a unique opportunity to advance the understanding of subduction zone earthquakes, as they can incorporate geodetically inferred spatiotemporal variation of tectonic loading within a finite-sized domain (e.g., Allison & Dunham, 2018; Duan & Oglesby, 2006; Erickson & Dunham, 2014; Takeuchi & Fialko, 2012), rather than a half-space as assumed in boundary element/integral methods. Volumetric SEAS simulations can also handle complex fault geometry (e.g., Liu et al., 2020; Mia et al., 2024) and heterogeneous material properties (e.g., Kaneko et al., 2011; Thakur & Huang, 2021; Yun et al., 2025). Although volumetric SEAS simulations require higher computational costs, advances in parallel computing, often utilizing high-performance computing (HPC), enable volume-discretized SEAS simulations with realistic on- and off-fault properties (e.g., Gabriel et al., 2025; M. Li et al., 2022; Liu et al., 2020; C. C. Pranger, 2020; Uphoff et al., 2023).

Previous community code verification exercises have shown that simulated slip histories of volumetric SEAS codes are sensitive to the loading scheme and the domain size (Erickson et al., 2020; Jiang et al., 2022; Lambert et al., 2025). Erickson and Dunham (2014) obtained comparable rupture evolutions across models with different domain sizes in their vertical strike-slip fault simulations. However, they changed the characteristic state evolution distance (D_{RS}, Eq. (1)) when they changed the domain size, making it unclear whether the rupture evolution would remain unchanged even under the same D_{RS} value. M. Li et al. (2022) tested two different loading methods and computational domain sizes using a vertical strike-slip fault and reported minimal impact on short- and long-term rupture characteristics. However, a systematic exploration of how different loading conditions affect modeled SEAS has not been conducted, particularly for non-vertical, non-planar faults, such as those in subduction zones.

In this study, we compare three different loading schemes utilized in previous studies and systematically examine their benefits and limitations. We model a thrust fault with a curved geometry embedded in an isotropic elastic computational domain. The "parallel" loading accounts for loading from both sides and the bottom, the "side push" loading assumes horizontal convergence, and the "subducting slab" loading imposes a constant velocity at the bottom of a finite-thickness slab. We examine the effects of domain size, slab thickness, and heterogeneity in elastic properties on modeled rupture and

deformation patterns. Parallel and side push loading schemes produce comparable recurrence intervals, average slip, stress drops, and rupture extents, whereas subducting slab loading produces distinct sequences with additional partial rupture earthquakes. The three loading schemes are clearly distinguished by their strain rate distributions within the computational domain, with different locations of strain localization. Among the three loading methods explored in this study, the subducting slab loading produces deformation patterns most consistent with observations, including minimal long-term vertical motion and clear afterslip and slow slip event signals. Across loading schemes, on-fault stressing rates and off-fault strain rates vary by 1-2 orders of magnitude, indicating that boundary conditions control deformation patterns in SEAS simulations. Although this study uses a volumetric method, such sensitivity to loading conditions is not necessarily limited to volumetric approaches. Future studies should therefore carefully consider potential loading-driven artifacts when designing and interpreting modeled slip sequences.

2 Model Setup

2.1 SEAS Simulations Using *Tandem*

We use the open-source volumetric SEAS simulation software *Tandem* (Gabriel et al., 2025; Uphoff et al., 2023) to explore different loading schemes. *Tandem* uses a symmetric interior penalty discontinuous Galerkin (SIPG) spatial discretization with the regularized formulation of the rate-and-state friction law (Dieterich, 1979; Lapusta et al., 2000; Ruina, 1983):

$$-\tau = a\sigma_n \sinh^{-1}\left[\frac{V}{2V_0}\exp\left(\frac{f_0 + b\ln\left(V_0\theta/D_{RS}\right)}{a}\right)\right] + \eta V, \tag{1}$$

where τ and σ_n are shear and normal stresses on the fault, respectively, V is the slip rate, V_0 is the reference slip rate, a and b are the rate-and-state parameters controlling direct and evolution effects, respectively, D_{RS} is the characteristic state evolution distance, f_0 is the reference friction coefficient, and θ is the state variable. We adopt the aging law (Dieterich, 1979) for the evolution of the state variable θ, given by

$$\frac{d\theta}{dt} = 1 - \frac{V\theta}{D_{RS}}. \tag{2}$$

The ODEs for the state variable are evolved using an embedded fifth-order Runge-Kutta scheme with a Dormand-Prince error controlled adaptive time stepping scheme. Support for the time integration method is provided by PETSc's TS object (Abhyankar et al., 2014; Balay et al., 1997, 2019).

We perform two-dimensional (2D) quasi-dynamic simulations, in which a radiation damping term ηV (Eq. (1)) approximates the inertial effect, with $\eta = \mu/2c_s$ being the half shear-wave impedance for shear modulus μ and shear-wave speed c_s (Rice, 1993). In most of the models, we assume a spatially constant $c_s = 3.464$ km/s and density $\rho = 2670$ kg/m^3, yielding a uniform constant value for μ of ~ 32 GPa.

2.2 Boundary Conditions and Loading Schemes

Volumetric SEAS methods allow prescribed boundary conditions to drive deformation in the elastic bulk material. *Tandem* supports three types of boundary conditions: 1) fault interface governed by rate-and-state friction law (black lines in Fig. 1), 2) free surface with zero traction (grey lines in Fig. 1), and 3) Dirichlet boundary condition with predefined displacements (red lines in Fig. 1). Note that *Tandem* does not consider "roller" boundary conditions (i.e., free-slip). We load the 2D elastic computational domain by prescribing the spatiotemporal evolution of displacement $\boldsymbol{u}_{BC}(x, y, t) = (u_x(t), u_y(t))$ along Dirichlet boundaries. In all three loading schemes, we fix the vertical extent of the domain to 200 km and assign a free surface boundary condition to the

surface (i.e., zero depth) and the bottom of the computation domain (i.e., 200 km depth). All three loading schemes require 800-900 CPUh to perform a 2,000 yr long SEAS simulation.

The first loading scheme considered in this study is "parallel loading" or "PL", where both ends of a parallelogram-shaped domain move opposite to each other parallel to a deep VS part of the fault (Fig. 1a). Within the domain, we embed an internal linear interface connected to the fault with the same uniform dip beneath the fault to apply loading from the bottom as well. This loading scheme is similar to that suggested by the community benchmark problem BP3 (Erickson et al., 2023), which aims to capture the concept of the "back-slip" approach (Savage & Prescott, 1978; Savage, 1983). We impose the displacement $\boldsymbol{u}_{BC}^{PL}$ along both Dirichlet boundaries beneath the fault and at both far-field edges:

$$\boldsymbol{u}_{BC}^{PL}(x,y,t) = \begin{cases} V_{pl}t(-\cos(\phi)/2, \sin(\phi)/2) & x > 0 \\ V_{pl}t(\cos(\phi)/2, -\sin(\phi)/2) & x < 0 \end{cases}, \tag{3}$$

where ϕ is the uniform dip angle of the Dirichlet boundaries. Because the dip angle of the fault changes toward the surface, stresses in the shallow crust are expected to become progressively more tensile in this scheme.

The second loading scheme, termed "side push loading" or "SPL", assumes horizontal velocities at both ends of a rectangular domain, while fixing far-field vertical motion to zero (Fig. 1b). Biemiller et al. (2024) utilized this type of loading in their exploration of the curvature in subduction zone rupture characteristics. The displacement time history imposed on the Dirichlet boundaries at both sides is:

$$\boldsymbol{u}_{BC}^{SPL}(x,y,t) = \begin{cases} (-V_{pl}t/2, 0) & x > 0 \\ (V_{pl}t/2, 0) & x < 0 \end{cases}. \tag{4}$$

There is no Dirichlet boundary beneath the fault in this loading scheme, and the entire interface, ranging from the surface to the bottom, is governed by the rate-and-state friction law.

In the last loading scheme considered in this study, termed "subducting slab loading" or "SSL", a slab of finite width (D) drives the relative plate motion, while the far-field displacements on the overriding plate are set to zero (Fig. 1c). This scheme mimics the kinematics of subduction zones. Kanda and Simons (2010) explored a similar loading scheme using dislocations in an elastic half-space, and Shreedharan et al. (2023) utilized it in their geodynamic simulations of the Hikurangi subduction zone in New Zealand. The displacement imposed on the Dirichlet boundaries is:

$$\boldsymbol{u}_{BC}^{SSL}(x,y,t) = \begin{cases} (0,0) & x = x_{end},\ y \geq y_f \\ V_{pl}t(\cos(\phi(\boldsymbol{x})), -\sin(\phi(\boldsymbol{x}))) & \text{otherwise} \end{cases}, \tag{5}$$

where $\phi(\boldsymbol{x})$ is the varying local dip angle at $\boldsymbol{x} = (x, y)$, x_{end} is the maximum x value on the slab, and y_f is the thickness of the far-field zero-displacement boundary layer. Unless otherwise mentioned, we use $D = 30$ km and $y_f = -D$. We discuss the effects of the slab thickness and y_f in more detail in the Section 6.1 and in Supplementary Text S1, respectively. Similar to the side push loading, the fault extends from the surface to the bottom of the domain.

2.3 Fault Geometry and Input Parameters

We assume a parabolic fault geometry $y = -Ax^2$ where y is the depth, x is the horizontal distance from the trench (in km), and $A = 3\times10^{-3}$ km^{-1} is the curvature. England and May (2021) showed that simple parabolic curves can approximate slab geometries in the major subduction zones. The effect of different A values in the subduction zone earthquake cycle has been thoroughly explored in Biemiller et al. (2024). We

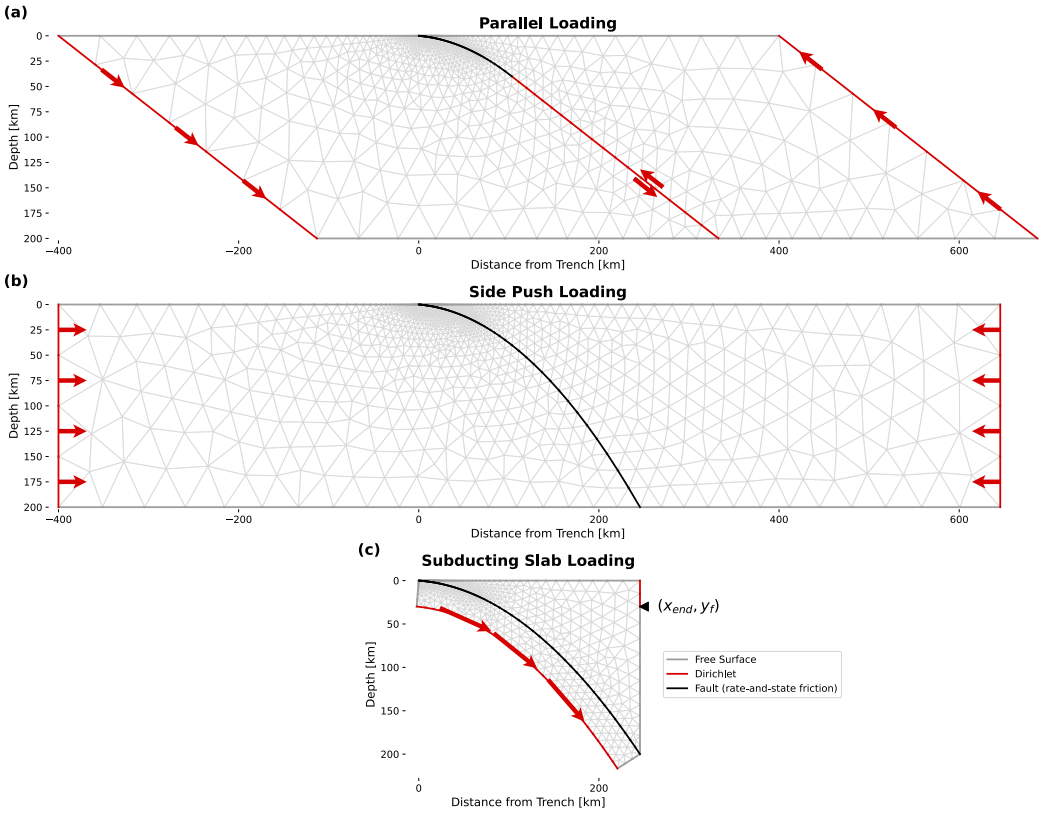

Figure 1. Model geometry and imposed boundary conditions for (a) the parallel, (b) the side push, and (c) the subducting slab loading schemes. Black lines indicate faults governed by the rate-and-state friction law, grey lines indicate free surface boundary conditions, and red lines indicate Dirichlet boundary conditions. Red arrows show the direction and relative magnitude of the imposed displacements: the length of arrows in each panel is proportional to the imposed velocity of $\|\boldsymbol{v}\| = V_{pl}/2$ for the parallel and the side push loading schemes and $\|\boldsymbol{v}\| = V_{pl}$ for the subducting slab loading. Black triangle in panel (c) marks the point (x_{end}, y_f) defined in Eq. (5).

shift the curve such that the point (12.91 km, −0.5 km) is translated to the origin (0 km, 0 km) to prevent zero dip angle at the surface:

$$y = -A(x + 12.91)^2 + 0.5. \tag{6}$$

The resulting geometry yields a dip of 5° at the surface, comparable to that of the northern Hikurangi subduction zone slab geometry (Williams et al., 2013). The vertical dimension (width) of the domain is kept at 200 km, while the horizontal dimension (length) of the domain is 800 km in parallel loading and ∼ 1000 km in side push loading. In subducting slab loading, a domain width of 200 km results in a domain length (x_{end}) of ∼ 245 km. The domain lengths in parallel and side push loading schemes are chosen to be 400 km distance between the fault and domain boundaries. To assess the effects of these choices, we perform two additional sets of models: (1) a side push loading model with a larger domain length of ∼1,800 km, and (2) a subducting slab model with an increased slab thickness (D) of 100 km. These models are denoted with the tag "L", where "L" stands for "Large", and are discussed in detail in Section 6.1. The effects of domain length for parallel loading are discussed in Erickson et al. (2023), and those for subducting slab loading (x_{end}) are discussed in Supplementary Text S1.

For most of the models shown in this study, we adopt simple input frictional properties from a SCEC community benchmark problem, BP3, tailored for dipping faults (Erickson et al., 2023), featuring spatially uniform background effective normal stress (σ_n^0) of 50 MPa and D_{RS} of 8 mm (Fig. S1). The rate-and-state parameters a, b determine a 15 km-wide velocity-weakening (VW) seismogenic layer ($a-b < 0$) underlain by a velocity-strengthening (VS; $a - b > 0$) layer (Fig. S1). We set the steady-state stress in the VS layer as the background shear stress (τ^0) and set the initial state variable to be consistent with the initial slip rate and the background shear stress. Unless otherwise noted, we use these spatially uniform input parameters, denoted as "base" models, as summarized in Table 1. The minimum process zone size and the nucleation size using these parameters are 455 m and 2.6 km, respectively.

In addition, we explore two sets of model setups to assess how each loading scheme affects rupture characteristics and deformation under different material/frictional conditions. The first set of simulations accounts for the effect of loading schemes in the presence of material heterogeneity. In these simulations, we adopt a simplified 2D velocity structure from Hansen and Schmandt (2017), consisting of a three-layered slab (crust, mantle, and asthenosphere) and a two-layered overriding plate (crust and mantle), and a low-velocity wedge (Fig. S2). We denote these models as "heterogeneous material" models and with the tag "VM", where "VM" stands for "Velocity Model". We use the same rate-and-state friction parameters on the fault as reported in Table 1. The minimum process zone size and the nucleation size using these parameters are 566 m and 3.2 km, respectively.

The other set of simulations accounts for depth-dependent background normal and shear stresses by resolving a spatially uniform stress tensor ($\boldsymbol{\sigma}^B$) onto the curved fault geometry, where $\boldsymbol{\sigma}^B$ is given by

$$\boldsymbol{\sigma}^B = \begin{bmatrix} \sigma_1 & 0 \\ 0 & \sigma_3 \end{bmatrix}. \tag{7}$$

This setup is modified from the high pore-fluid pressure scenario in Madden et al. (2022) (their scenario 6). We assume that the most compressive principal stress ($\sigma_1 = 40$ MPa) is horizontal and the least compressive principal stress ($\sigma_3 = 19.6$ MPa) is vertical. Resolving the spatially uniform $\boldsymbol{\sigma}^B$ onto the curved fault geometry (Eq. (6)) results in depth-dependent σ_n^0 and τ^0 that increase as the depth increases (dashed lines in Figs. S1a-b). We denote these models as "uniform $\boldsymbol{\sigma}^B$" models and with the tag "T", where "T" stands for "Tensor". All other parameters are the same as shown in Table 1. The minimum process zone size and the nucleation size using these parameters are 1 km and 5.7 km, respectively.

Table 1. Input parameters used in the SEAS models using *Tandem*. See Table S1 for input parameters for models with depth-dependent stresses.

Symbol	Parameter	Value
a	Rate-and-state parameter, direct effect	0.025 - 0.010
b	Rate-and-state parameter, evolution effect	0.015
D_{RS}	Characteristic state evolution distance	8 mm
σ_n^0	Background effective normal stress	50 MPa
τ^0	Background shear stress	26.54 MPa
c_s	Shear wave speed *	3464 m/s
ρ	Density *	2670 kg/m^3
ν	Poisson's ratio	0.25
μ	Shear modulus *	32.04 GPa
f_0	Reference coefficient of friction	0.6
V_0	Reference slip rate	10^{-6} m/s
V_{init}	Initial slip rate	10^{-9} m/s
V_{pl}	Plate loading rate	10^{-9} m/s
W	Seismogenic zone width	15 km
L_f	Rate-and-state fault length	40 km

* Spatially varies for heterogeneous material model (see Fig. S2).

In models denoted using the tag "C", an abbreviation for "Creep", we assign VS rheology throughout the fault, allowing it to creep freely at the assumed plate loading rate (V_{pl}). These models illustrate long-term strain and stress accumulation patterns arising from different loading methods. These models require ∼1 CPUh to perform a 2,000 yr long simulation. We apply this rheology to the larger domain size models (category "L") and the uniform $\boldsymbol{\sigma}^B$ models (category "T"), denoted with tags "LC" and "TC", respectively. A complete list of the setup and their tags is shown in Table 2.

We discretize the fault using triangular elements with 100 m edge length on the velocity-weakening seismogenic layer and varying element sizes from 200 m to 5 km on the velocity-strengthening part of the fault. We use a higher-order fault basis with polynomial degree 6, resulting in the effective element size of ∼17 m at the seismogenic zone (Uphoff et al., 2023). This resolves the minimum critical length scale by 26 cells in the default setup, 59 cells in uniform $\boldsymbol{\sigma}^B$ models, and 33 cells in models with 2D velocity structure. We verify the resolution of our models by comparing them with models using a mesh with twice the on-fault resolution (50 m edge length) and find that the major on- and off-fault properties remain unchanged (Fig. S3). The mesh element size gradually increases to 50 km towards the domain edge at ∼400 km away from the fault.

2.4 Metrics for Systematic Comparisons

To systematically compare the three loading schemes, we apply an automated earthquake-classification algorithm that identifies earthquake onsets and terminations based on a threshold slip rate (Yun et al., 2025). We use a threshold slip rate of 1 cm/s. Slip events with slip rates that are lower than this but higher than the plate loading rate (V_{pl}) are identified as slow slip events (SSEs). To examine earthquake characteristics produced by each loading scheme, we compute average slip, rupture extent, average static stress drop, and recurrence interval. We measure the extent of the rupture as the length of the fault that slipped more than 1 cm, and the recurrence interval as the time between earthquakes. We adopt an energy-related averaging method for the stress drop calculation (Noda et al., 2013).

Table 2. Descriptions of all explored model setups and the corresponding tags used in this study. VS: velocity-strengthening.

Model Tag	Loading Scheme	Description
PL	Parallel Loading	Base setup
PL-C		Base setup, fully VS rheology
PL-VM		Heterogeneous material
PL-TC		Uniform $\boldsymbol{\sigma}^B$, fully VS rheology
SPL	Side Push Loading	Base setup
SPL-C		Base setup, fully VS rheology
SPL-L		Base setup, larger domain length
SPL-LC		Base setup, larger domain length, fully VS rheology
SPL-VM		Heterogeneous material
SPL-TC		Uniform $\boldsymbol{\sigma}^B$, fully VS rheology
SSL	Subducting Slab Loading	Base setup
SSL-C		Base setup, fully VS rheology
SSL-L		Base setup, larger slab thickness (D)
SSL-LC		Base setup, larger slab thickness (D), fully VS rheology
SSL-VM		Heterogeneous material
SSL-TC		Uniform $\boldsymbol{\sigma}^B$, fully VS rheology

To assess domain deformation patterns, we calculate the invariants of the strain rate tensor $\dot{\boldsymbol{\epsilon}}$. The first invariant $\dot{\boldsymbol{\epsilon}}_{\mathrm{I}} = \mathrm{Tr}\,(\dot{\boldsymbol{\epsilon}})$ illustrates how each loading method alters volumetric strain while the second invariant of the deviatoric strain rate tensor ($\dot{\boldsymbol{\epsilon}}'$) defined by

$$\dot{\boldsymbol{\epsilon}}'_{\mathrm{II}} = \sqrt{\frac{1}{2}\left(\dot{\epsilon}'^2_{11} + \dot{\epsilon}'^2_{22} + 2\dot{\epsilon}'^2_{12}\right)} \tag{8}$$

measures changes in shear strain rate driven by loading. We compare the effects of each loading scheme on the strain rate distribution in Section 5.

Since *Tandem* assumes that the material is isotropic, we can convert the strain tensor to the stress tensor $\boldsymbol{\sigma}$ based on Hooke's law. Note that the total stress in the computational domain ($\boldsymbol{\sigma}(\boldsymbol{u})$) is the sum of the background stress ($\boldsymbol{\sigma}^B$), defined by the initial parameters, and changes in stress due to deformation ($\boldsymbol{\sigma}^D(\boldsymbol{u})$), i.e.,

$$\boldsymbol{\sigma}(\boldsymbol{u}) = \boldsymbol{\sigma}^B + \boldsymbol{\sigma}^D(\boldsymbol{u}), \tag{9}$$

where $\boldsymbol{u}$ is the displacement. We compare the effects of each loading scheme on the principal stresses and their orientations in Section 6.3.

3 Earthquake Characteristics on Fault

Figure 2 shows rupture patterns resulting from the three loading schemes. After a few cycles, all three models (PL, SPL, and SSL) yield quasi-repeating, spun-up cycles consisting of a system-size earthquake that ruptures the entire fault, followed by a smaller earthquake that terminates at ~ 8 km depth. Earthquakes in these models always nucleate from the bottom of the seismogenic layer and propagate toward the free surface. Models PL and SSL generate spontaneous slow slip events preceding large earthquakes. Based on the repeatability of the cycle, we discard the initial 9 (model PL), 7 (model SPL), or 15 (model SSL) earthquakes, considering them as the spin-up phase (grey lines in Fig. 2). We only consider the spun-up part of the cycle for further investigation.

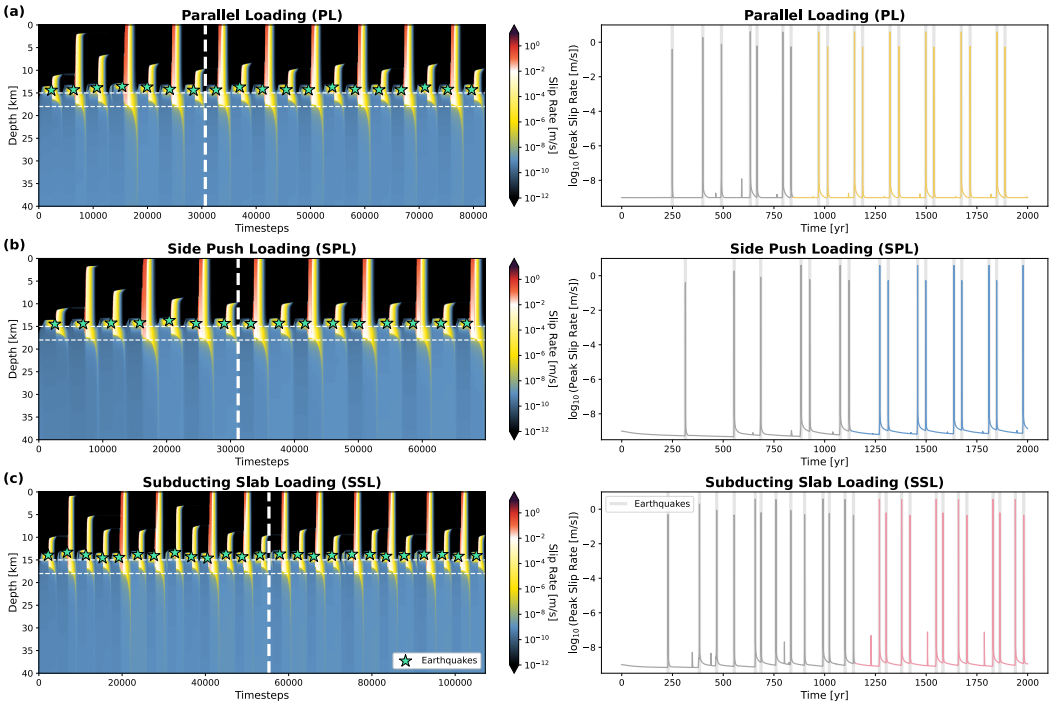

Figure 2. Spatiotemporal evolution of slip rate (left column) and peak slip rates (right column) obtained from (a) the parallel (model PL), (b) the side push (model SPL), and (c) the subducting slab (model SSL) loading schemes. Green stars in the left column and light grey vertical bars in the right column mark earthquakes. The colored lines in the right column indicate the spun-up earthquake cycles included in the further analyses. Vertical white dashed lines in the left column mark the transition point from the spin-up phase to the spun-up cycle. Horizontal dashed lines in the left column indicate depths at which the frictional rheology transitions between VW and VS, same as those in Figure S1.

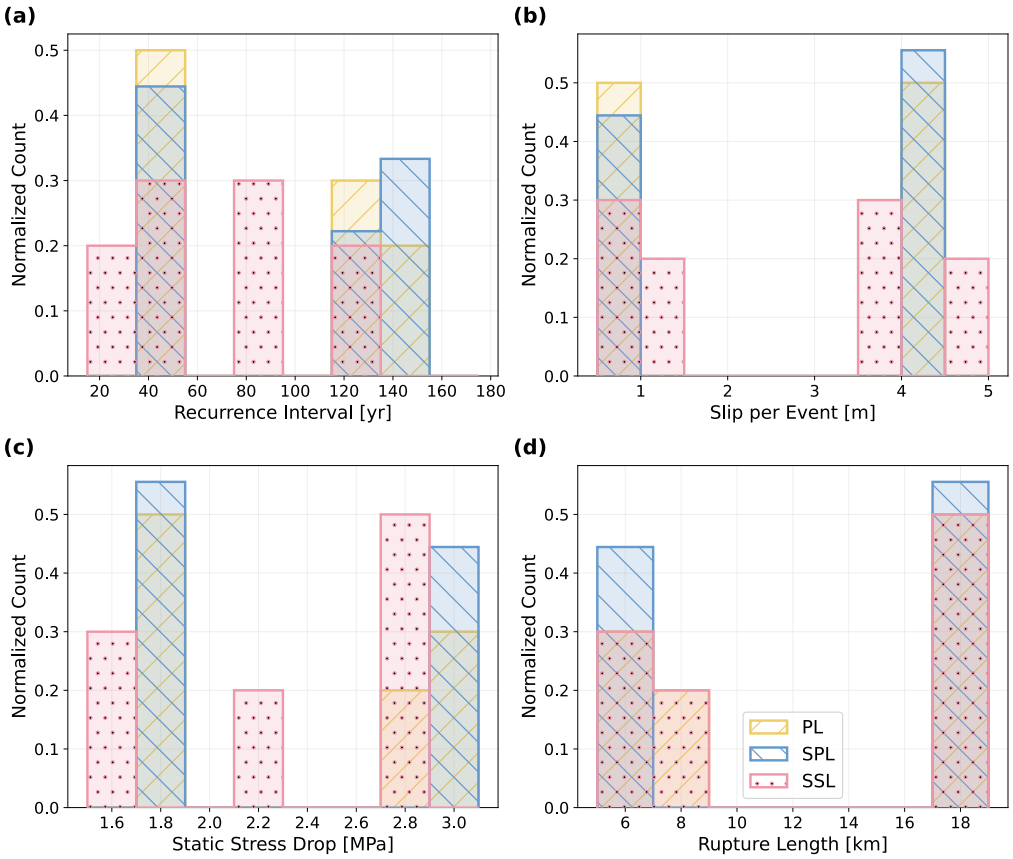

Figure 3. Earthquake characteristics calculated from the parallel (model PL; yellow, forward hatched), the side push (model SPL; blue, backward hatched), and the subducting slab (model SSL; pink dotted) loading schemes: (a) Recurrence interval, (b) average slip, (c) average static stress drop, and (d) rupture extent.

The characteristics of earthquakes produced by models PL and SPL are largely comparable, while model SSL shows different patterns. Figure 3 shows recurrence interval, average slip, average static stress drop, and rupture extent from all three models. Models PL and SPL show a bimodal distribution of earthquake characteristics consisting of larger earthquakes with ∼4 m slip and ∼2.9 MPa stress drop and smaller earthquakes with ∼1 m slip and ∼1.8 MPa stress drop. The recurrence interval and stress drop pattern reveal that the cycles of model SSL consist of two sub-cycles, each consisting of one system-size earthquake and one partial rupture earthquake, but the two partial ruptures differ in size and recurrence patterns. One group of partial ruptures is roughly comparable to those in models PL and SPL, while the other group of partial ruptures shows an intermediate recurrence interval of ∼85 yr and stress drop of ∼2.1 MPa. The maximum recurrence interval varies the most across the three models, ranging from 130 yr to 150 yr, while the other parameters are more comparable except for the emergence of the intermediate-size partial ruptures in model SSL. The sensitivity of long-term variables, such as recurrence interval, to loading methods is consistent with findings from previous community benchmark exercises (Erickson et al., 2020; Jiang et al., 2022).

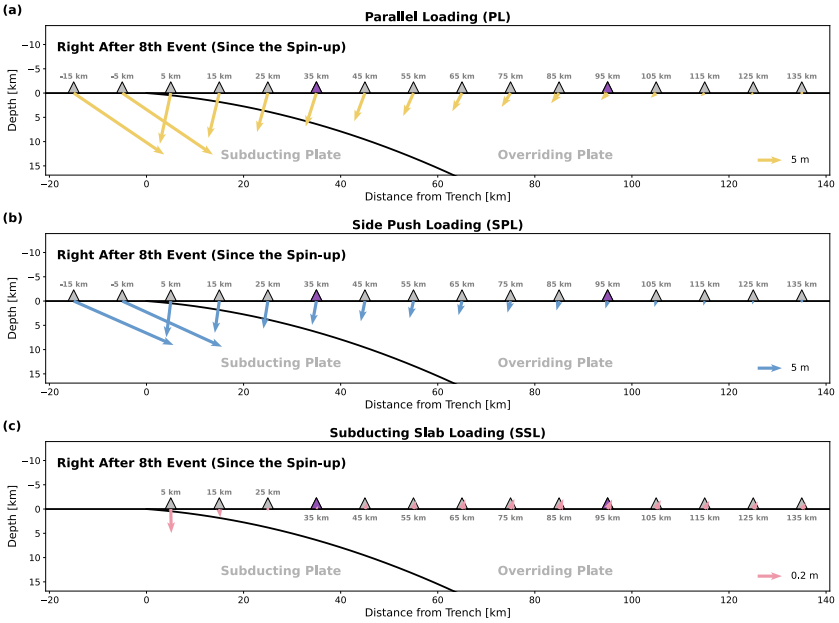

Figure 4. Accumulated surface displacement after eight earthquakes since the spin-up phase, produced by (a) the parallel (model PL), (b) the side push (model SPL), and (c) the subducting slab (model SSL) loading schemes. All displacements are relative to a far-field station located at 245 km from the trench. For visual clarity, the arrow size is exaggerated, and its scale is shown in the bottom right corner. Triangles indicate the station locations that record synthetic displacements, and those colored in purple are the stations shown in Figure 5. See Supplementary Movie 1 for the full evolution of surface displacement throughout eight earthquakes.

4 Surface Displacement Patterns

Surface displacements exhibit more striking differences between the three models. Figure 4 shows the accumulated surface displacements relative to a far-field station 245 km (i.e., x_{end} in Eq. (5)) from the trench after eight system-size earthquakes since the end of the spin-up phase. The stations on the overriding plate show a trench-ward, subsiding motion in models PL and SPL, while almost no displacements accumulate in model SSL. This indicates that coseismic displacements do not cancel out interseismic displacements in models PL and SPL, which is inconsistent with the expectations from a purely elastic kinematic assumption (Savage, 1983).

Individual displacement time series at two stations on the overriding plate better illustrate how displacement accumulates over time (Fig. 5). In all models, surface stations move away from the trench during the interseismic period and towards the trench coseismically. Coseismic trenchward motion and interseismic landward motion are consistent with horizontal displacements expected from elastic simulations (Kanda & Simons, 2010; Luo et al., 2025). However, coseismic trenchward motions in models PL and SPL exceed interseismic landward motions, leaving permanent trenchward displacements in both models. In contrast, coseismic and interseismic displacements cancel each other in model SSL once it enters the cycle-invariant regime. Similarly, models PL and SPL produce permanent subsidence on the overriding plate, whereas model SSL does not produce long-term permanent displacements once it is spun up. Minimal long-term accumulation of vertical displacements in model SSL, unlike the other two models, resembles geodetic observations in subduction zones (e.g., Jolivet & Frank, 2020; Woods et al.,

2024). Since we applied the far-field correction for all displacement fields shown in Figures 4 and 5, the long-term accumulation of surface displacements in models PL and SPL is an artifact caused by the loading conditions. The continuous strain accumulation over time in models PL and SPL suggests that the apparently spun-up cycles in these models may eventually change as simulations run longer.

The surface displacements in Figure 5 not only show coseismic and interseismic deformation patterns, but also capture the afterslip and SSEs (Fig. 6). For example, the vertical displacement recorded at the station located 95 km from the trench in model SSL (red lines in Fig. 5c) exhibits more curved interseismic deformation, forming a "bulging" pattern, unlike the linear, "sawtooth" patterns recorded at the near-field station (black lines in Fig. 5c). We find that this "bulging" pattern in the far-field vertical displacement arises from afterslip, which causes additional uplift motion, continued from the coseismic uplift (Fig. 6). A large, system-size earthquake generates strong afterslip, causing uplift motion for the entire 40-year interseismic period. This non-constant uplift rate creates a curved displacement pattern observed in Figure 5. In contrast, a smaller, partial-rupture earthquake produces less prominent afterslip, insufficient to overcome the interseismic subsidence imposed by the boundary condition. This drives the overall subsiding displacement pattern, keeping the net vertical displacement level similar throughout multiple earthquake cycles. Although the signature of afterslip is less prominent in horizontal velocity, a trenchward displacement caused by the afterslip lasts for ~ 5 years after system-size earthquakes (Fig. 6c).

Figure 6 also shows that the surface stations capture SSE signals well, although their rupture is confined to a relatively small area (13-18 km depth). The SSE between earthquakes 20 and 21 causes a clear trenchward velocity in both surface stations. Vertical motion due to the SSE depends on station location: a near-field station shows uplift, whereas a far-field station continues to subside with an increased subsidence rate. The uniform trenchward horizontal motion, uplift near the trench, and the subsidence at down-dip of the slip patch are consistent with horizontal and vertical displacements of natural SSEs observed by GNSS and pressure gauge data (e.g., Ito et al., 2013; Wallace et al., 2016).

Figure 7 shows that surface velocities are comparable across different models early in the interseismic period (10% of the recurrence interval), but exhibit variability late in the cycle (99% of the recurrence interval). In the early interseismic period, models PL, SPL, and SSL (solid lines in Fig. 7a) exhibit landward motion near the trench, which gradually decreases away from the trench, along with a transition from subsidence to uplift from near-trench to far-field. In the late interseismic period, model SSL shows notably higher landward velocity, compared to models PL and SPL (Fig. 7b). Late interseismic vertical velocities from the three models are more distinctive: model SSL yields a relatively smaller uplift rate near the trench and consistent subsidence across all distances, while models PL and SPL show little vertical motion at distances larger than $\sim$ 100 km from the fault. The displacement patterns shown in Figure 7 are largely consistent with those computed using elastic dislocation models (e.g., Kanda & Simons, 2010; Luo et al., 2025; Trubienko et al., 2013), but show more variability in the near-trench vertical velocities, particularly during the late interseismic period.

5 Distribution of Strain and Stress

Figure 8 shows invariants of the strain rate tensor and their principal orientations for all three loading schemes using fully VS rheology (category "C"), after 2,000 yr of simulation time. Positive (negative) sign of the first invariant of the strain rate tensor $\dot{\boldsymbol{\epsilon}}_{\mathrm{I}}$ indicates dilatation (compaction). Models PL-C and SPL-C accumulate considerable dilatation at the surface above the trench. In model PL-C, relatively strong compaction occurs near the transition between the fault and the bottom Dirichlet boundary at $\sim$40 km

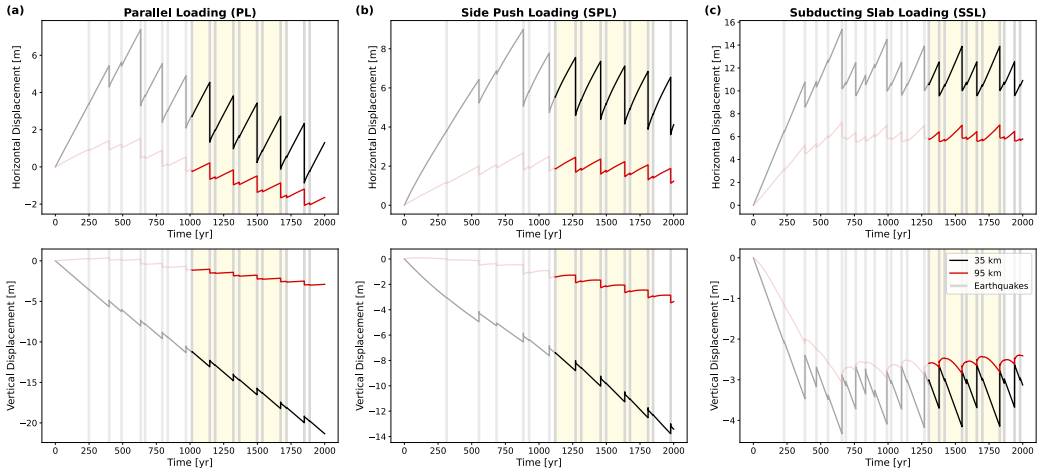

Figure 5. Time series of horizontal (top row) and vertical (bottom row) surface displacements obtained from (a) the parallel (model PL), (b) the side push (model SPL), and (c) the subducting slab (model SSL) loading schemes. Black (and grey) curves show displacements at a station above the locked part of the fault (35 km from the trench) while red (and pink) curves show those at a station further landward (95 km from the trench). The locations of these two stations are marked as purple triangles in Figure 4. Lighter colored lines (grey and pink) indicate the spin-up phase. Yellow shaded areas show the time range in which we compute the displacement accumulation in Figure 4. All displacements are relative to a far-field station located at 245 km from the trench. Light grey vertical bars mark earthquakes.

depth (black and red lines in Fig. 1a), whereas the rest of the domain is weakly dilating. Most parts of the domain in model SPL-C show compaction with varying degrees, being more compressive surrounding the fault and at the far boundary, where horizontal shortening is applied (Fig. S4c). In contrast, model SSL-C exhibits little change in volumetric strain within the overriding plate, while yielding compaction along the slab surface and a minor dilatation at the lower part of the slab.

The second invariant of the deviatoric strain rate tensor $\dot{\boldsymbol{\epsilon}}'_{\mathrm{II}}$ (Eq. (8)) illustrates the intensity of shear deformation (bottom row of Fig. 8). Similar to the first invariant pattern, model SPL-C shows distributed shear across most of the regions, while model PL-C exhibits a stronger shear accumulation near the fault, which tapers towards the edges of the domain (Fig. S4b). Model SSL-C shows localized shear within the subducting slab and minimal shear deformation within the overriding plate.

Lastly, we examine how the stressing rate evolves on the fault under different loading schemes (Fig. 9). Note that with fully VS rheology, fault creeps without accumulating stress. Thus, a non-zero stressing rate implies stress accumulation over time due to the loading, possibly driving earthquake cycles away from converging toward a cycle-invariant behavior, i.e., "limit cycle" (Lapusta & Liu, 2009; C. Pranger et al., 2022; S. Wang, 2024). In model PL-C, we observe a significant normal stressing rate ranging from -0.5 to 6 kPa/yr and shear stressing rate from -0.3 to 3 kPa/yr. Considering that the stress drop in the model PL is ∼1-3 MPa, the stressing rate of a few kPa/yr is significant enough to alter the rupture characteristics when accumulated for thousands of years. In contrast, models SPL-C and SSL-C show stressing rates that are 1-2 orders of magnitude lower than those in model PL-C. The stressing rates in models SPL-C and SSL-C correspond to ∼10% and ∼1% of the coseismic stress drop, respectively. Model SSL-C, in particular, exhibits decreasing stressing rates over time, implying that it is likely to converge to a limiting

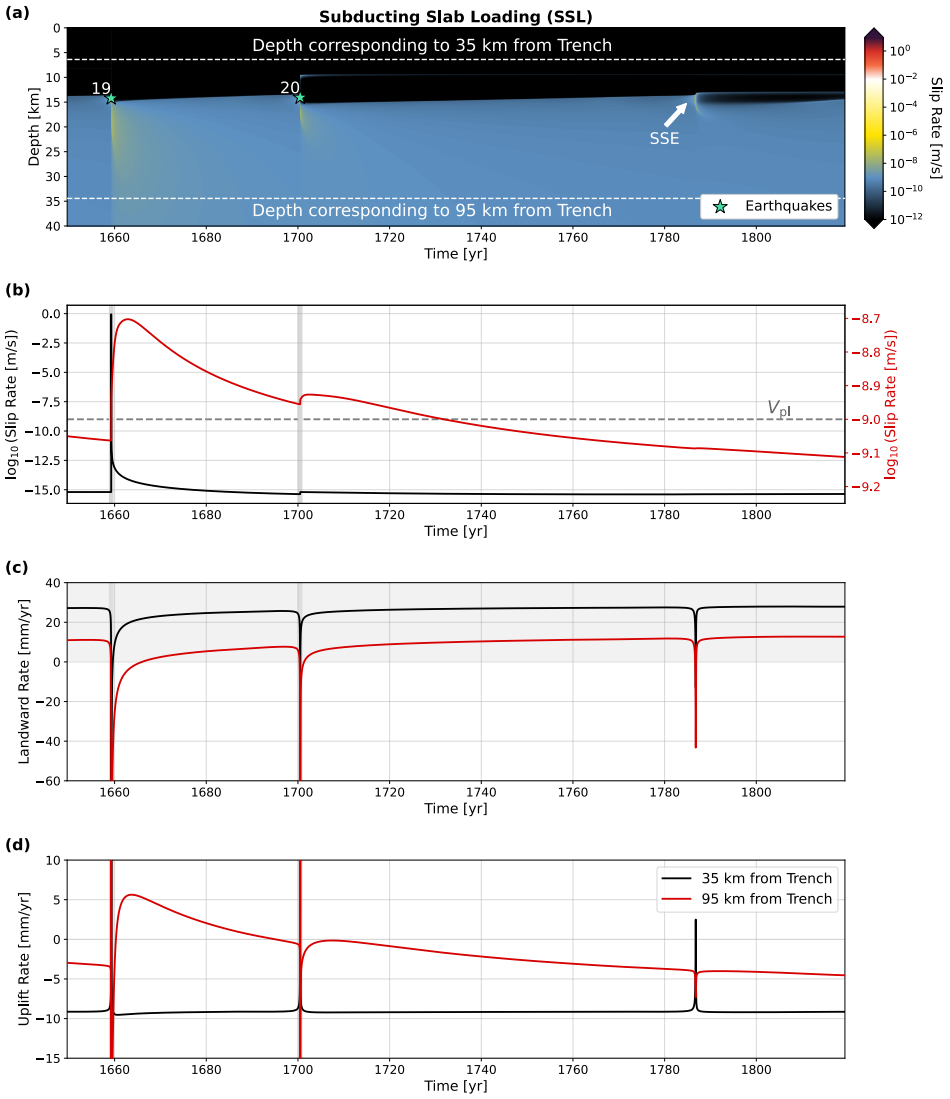

Figure 6. Zoomed-in view of the slip rate and surface velocity evolution during the interseismic period in model SSL. (a) Spatiotemporal evolution of slip rate between earthquakes 19 and 21. Green stars mark earthquakes, where earthquake 19 is a system-size earthquake and earthquake 20 is a partial-rupture earthquake. Horizontal dashed lines indicate fault depths corresponding to 35 km and 95 km from the trench. (b) Time series of slip rate at 6.3 km (black) and 34.4 km (red) depths, which correspond to 35 km and 95 km from the trench, respectively. Grey horizontal dashed line indicates the imposed plate loading rate, V_{pl}. For better visibility, we exaggerated the vertical axis of the slip rate time series at 34.4 km depth. See the axis ticks on the right-hand side. (c-d) Landward (c) and uplift (d) rates recorded at two surface stations located 35 km (black) and 95 km (red) from the trench. The shaded area marks positive landward and uplift rates. Grey vertical bars in panels (b-d) indicate earthquakes.

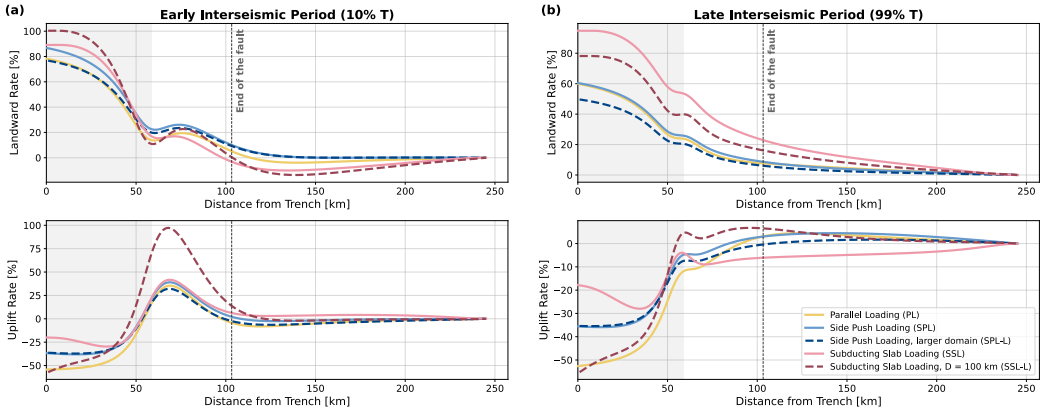

Figure 7. (a) Early and (b) late interseismic landward (top row) and uplift (bottom row) deformation rates at the surface as a function of distance from the trench, computed from all explored models: the parallel loading (model PL), the side push loading with different domain lengths (models SPL and SPL-L), and the subducting slab loading with different D values (models SSL and SSL-L). Early and late interseismic periods correspond to 10% and 99% of the recurrence interval, T, respectively. Landward and uplift rates are expressed as a percentage of the convergence rate (V_{pl}) imposed at the far boundaries. The grey shaded area and the vertical grey dashed line indicate the horizontal extents of the frictionally locked part of the fault and the end of the fault in the parallel loading scheme, respectively. All displacements are relative to a far-field station located at 245 km from the trench.

cycle less affected by artifacts from loading methods. This behavior is consistent with the evolution of earthquake properties: the final 9 system-size earthquakes in model PL show gradually decreasing recurrence intervals and stress drops, whereas those in model SSL remain nearly constant (Fig. S5).

6 Discussion

6.1 Effects of Domain length and Slab Thickness

Previous studies reported that the domain size or the slab thickness (D) can affect modeled earthquake cycles. Using kinematic elastic dislocation models comparable to the subducting slab loading configuration, Kanda and Simons (2010) showed that slab thickness alters surface displacements, particularly the vertical displacement. They report migration of the hinge line, the location where vertical velocity is zero, and an increase in horizontal velocity as slab thickness increases. In contrast, the locations of peak vertical velocity and horizontal velocity pattern as a function of distance from trench remain similar across different slab thicknesses.

We find that the slab thickness in the subducting slab loading scheme significantly affects both on- and off-fault deformation patterns, while the domain length in the side push loading scheme has only a moderate influence on them. By comparing models SPL (domain length of ∼1000 km) and SPL-L (domain length of ∼1800 km), we find that the domain length in the side push loading scheme primarily affects horizontal displacement (Fig. 7) and the recurrence interval of earthquakes (Fig. S6). Model SPL-L, compared to model SPL, produces a slightly lower landward velocity and a larger recurrence interval. In contrast, uplift rate, average slip, stress drop, and rupture lengths are com-

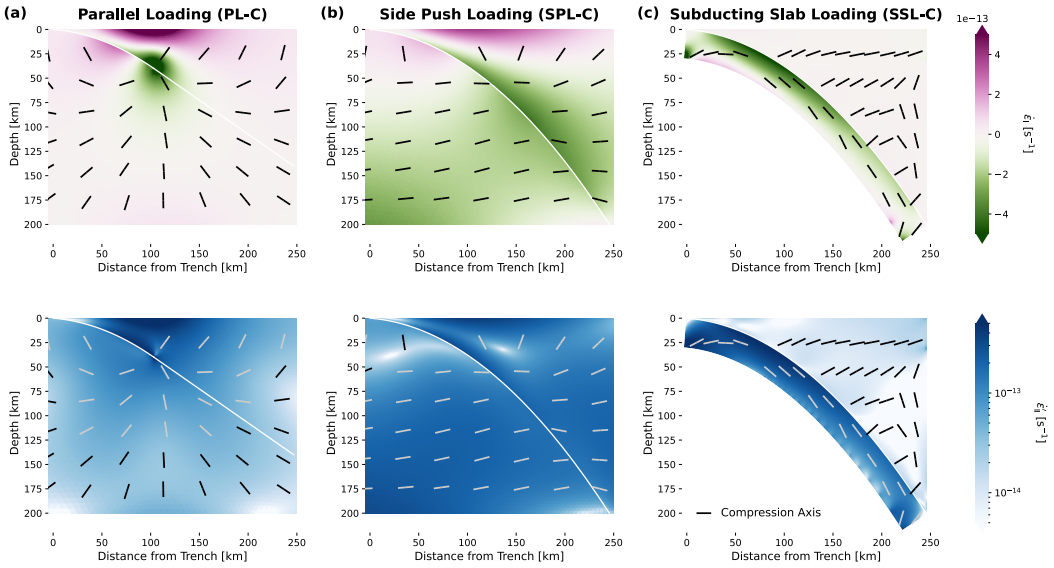

Figure 8. Invariants of strain rate tensors computed from (a) the parallel (model PL-C), (b) the side push (model SPL-C), and (c) the subducting slab (model SSL-C) loading schemes: (top row) First invariant of the strain tensor $\dot{\boldsymbol{\epsilon}}_{\mathrm{I}}$ and (bottom row) second invariant of the deviatoric strain tensor $\dot{\boldsymbol{\epsilon}}'_{\mathrm{II}}$ (Eq. (8)). Negative $\dot{\boldsymbol{\epsilon}}_{\mathrm{I}}$ indicates compression, and vice versa. Black and red bars indicate principal strain rate axes. White curves mark the fault and bottom Dirichlet boundary in model PL. The colorbar for the $\dot{\boldsymbol{\epsilon}}_{\mathrm{I}}$ is saturated at $\pm 5 \times 10^{-13}$ s^{-1} and that for the $\dot{\boldsymbol{\epsilon}}'_{\mathrm{II}}$ is saturated at 5×10^{-15} and 5×10^{-13} s^{-1}. We truncate models PL-C and SPL-C horizontally to match the spatial range of model SSL-C. Strain rate fields for the full domain in models PL-C and SPL-C are shown in Figure S4.

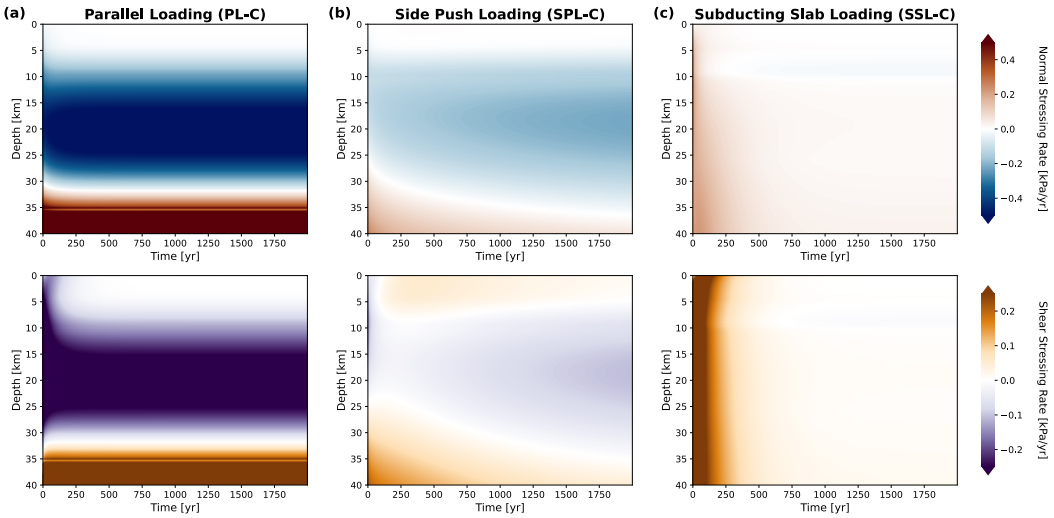

Figure 9. Stressing rates on the fault computed from (a) the parallel (model PL-C), (b) the side push (model SPL-C), and (c) the subducting slab (model SSL-C) loading schemes: (top row) Normal stressing rate and (bottom row) shear stressing rate. A positive normal stressing rate indicates stronger compression. The colorbar is saturated at ±0.5 kPa/yr for the normal stressing rate and ±0.25 kPa/yr for the shear stressing rate.

parable between models SPL and SPL-L. The sensitivity of the modeled recurrence interval on the domain size is consistent with previous findings (Jiang et al., 2022).

Comparing models SSL (D = 30 km) and SSL-L (D = 100 km) shows that the slab thickness in the subducting slab loading scheme significantly alters all rupture characteristics explored in this study (Fig. S7). Using a thicker slab (model SSL-L) produces a repeating earthquake cycle consisting of a system-size earthquake and two subsequent partial-rupture earthquakes. System-size earthquakes in model SSL-L yield larger slip ($>$ 6 m), but comparable stress drop ($\sim$2.8 MPa), compared to model SSL. SSEs preceding large earthquakes emerge in both models. In addition, models SSL and SSL-L produce notably different horizontal and vertical surface velocity patterns (Fig. 7). Horizontal velocity distribution as a function of distance from the trench is similar between the two models, while model SSL-L shows a larger amplitude during the early interseismic period and a smaller amplitude during the late interseismic period. As reported in Kanda and Simons (2010), the peak location of vertical velocity remains similar between the two models, while the hinge line in the early interseismic period is slightly migrated towards the trench in model SSL-L. The difference in the vertical velocity between the two models is more prominent above the locked part of the fault.

We find similar normal and shear stressing rates on the fault between models SPL-C and SPL-LC (Fig. S8). The two models also exhibit similar strain rate distribution, but with reduced amplitudes in model SPL-L (Figs. 8 & S9a). This is expected because increasing the distance between the fault and the far-field boundaries distributes the same imposed boundary displacement over a larger length scale, thereby reducing the strain rate.

Models SSL-C and SSL-LC show a similar pattern of strain rate invariance, with a strong compaction near the slab interface and dilatation at the bottom of the slab (Figs. 8c & S9b). However, the magnitude of the strain rate is notably higher in model SSL-LC, about three times that of model SSL-C. In addition, the amplitude of stressing rates in model SSL-LC is larger than in model SSL-C (Fig. S8). Such fundamental differences between models SSL-C and SSL-LC may be related to a change in the system's effective rigidity, which is proportional to the cube of the slab thickness (Walcott, 1970).

6.2 Effects of Heterogeneous Elastic Properties

We incorporate spatially varying elastic parameters (Fig. S2) and find that the key results of this study are robust across various assumed material properties. The heterogeneous material models (PL-VM, SPL-VM, and SSL-VM) produce similar earthquake cycles consisting of a large, system-size earthquake followed by a partial rupture earthquake. SSEs observed in model PL are not present in model PL-VM. Compared to their uniform-material-property counterparts, the recurrence interval of large earthquakes is smaller in models with varying elastic parameters. The three loading schemes with spatially varying material properties produce comparable average slip, stress drops, and rupture lengths (Fig. S10).

Displacement patterns across the computational domain, including the permanent accumulation of surface displacements and the perpetual stressing rates under parallel and side push loading schemes, remain the same in models with a 2D velocity structure. These results suggest that the differences among the models reported in this study are likely inherent to the loading methods, rather than to the specific choices of material properties.

6.3 Comparison with Observed Earthquake Rupture Characteristics and Stress Distributions

Seismic and geodetic observations have revealed complex focal mechanisms of subduction zone earthquakes, implying heterogeneous stress conditions (e.g., Asano et al., 2011; Pardo et al., 2002). Earthquake focal mechanisms also provide important constraints on the orientations of the principal stresses, the fault strength, and the differential stress surrounding the megathrust. For example, the plunge angle of the maximum compressive stress axis before large megathrust earthquakes is estimated to be 25-30° in the Japan Trench (Hasegawa et al., 2011) and varies from 10° to 50° worldwide (Hardebeck, 2015), pointing toward the slab interface. Principal stresses often rotate after large megathrust earthquakes, such as the 2011 M_w 9.1 Tohoku-Oki, Japan, earthquake (e.g., Hasegawa et al., 2012) and 2004 M_w 9.2 Sumatra-Andaman, Indonesia, earthquake (e.g., Hardebeck, 2012). Along the Japan Trench, some aftershocks of the 2011 M_w 9.1 Tohoku-Oki earthquake exhibit dip angles 5–10° steeper than the megathrust interface, suggesting that the megathrust may not be substantially weaker than the surrounding faults (Zhan et al., 2012).

Volumetric SEAS models facilitate comparison with observationally constrained stress regimes in subduction zones as they consistently evaluate stress distributions in the domain surrounding the fault. For example, using uniform $\boldsymbol{\sigma}^B$ models (PL-TC, SPL-TC, and SSL-TC), we explore the principal stress orientation produced by each loading method (Fig. 10). We record the plunge angle of the principal stress axes, measured counterclockwise from the vector $(-1, 0)$. By design, plunge angles greater than 90° indicate a plunge away from the slab interface, and vice versa. We note that assuming a uniform $\boldsymbol{\sigma}^B$ as an initial condition results in a prolonged spin-up phase. To reach steady-state creep at the imposed convergence rate (V_{pl}), models require several thousand years (models PL-TC and SSL-TC) or even over 20,000 yrs.

We find that the plunge angle of the maximum compressive stress axis (σ_1) differs significantly across the three loading schemes. Using the parallel loading (model PL-TC), the average plunge angle is over 90°, implying that σ_1 in this model is dominantly subparallel to the slab interface, instead of pointing towards it. Using side push loading (model SPL-TC), we estimate $\sim 50°$ plunge, which is on the upper limit of the observationally inferred σ_1 orientation. The subducting slab loading (SSL-TC) produces σ_1 axes plunging $\sim 25°$ towards the slab interface, consistent with that inferred from earthquake focal mechanisms (10-50°). This result suggests that the subducting slab loading is suitable for modeling stress evolution in subduction zones throughout earthquake cycles.

In addition, we estimate optimal fault orientations across the domain and compute their normalized slip tendency $\tau/f_0\sigma_n$ (Morris et al., 1996) to assess how each loading scheme modulates failure conditions on these planes (Fig. S11). To exclude the effects of the spin-up phase, we only focus on how the normalized slip tendency changed during the last 200 years of simulation time, where stress distribution is relatively steady (Fig. 10). Similar to the strain rate distribution (Fig. 8), normalized slip tendency in models PL-TC and SPL-TC increases near the fault and decreases near the surface on the overriding plate. In model SSL-TC, the normalized slip tendency is highly localized near the bottom of the subducting slab, where bending stress accumulates. We note that one of the optimal failure plane orientations lies at an angle of $\sim 20°$ in model PL-TC, 10-20° in model SPL-TC, and 5-20° in model SSL-TC to the slab interface (Fig. S11d). These angles, particularly those in model SSL-TC, are somewhat consistent with the 5-10° angle between the megathrust and the anomalously steep aftershock nodal planes in the Japan Trench, reported in Zhan et al. (2012). This result supports the view that the aftershocks occurred on optimally oriented subfaults, although other possible explanations, such as a geometrically complex megathrust interface, cannot be ruled out. These results highlight the potential of volumetric SEAS models with realistic loading conditions for broader applications in subduction faulting mechanics.

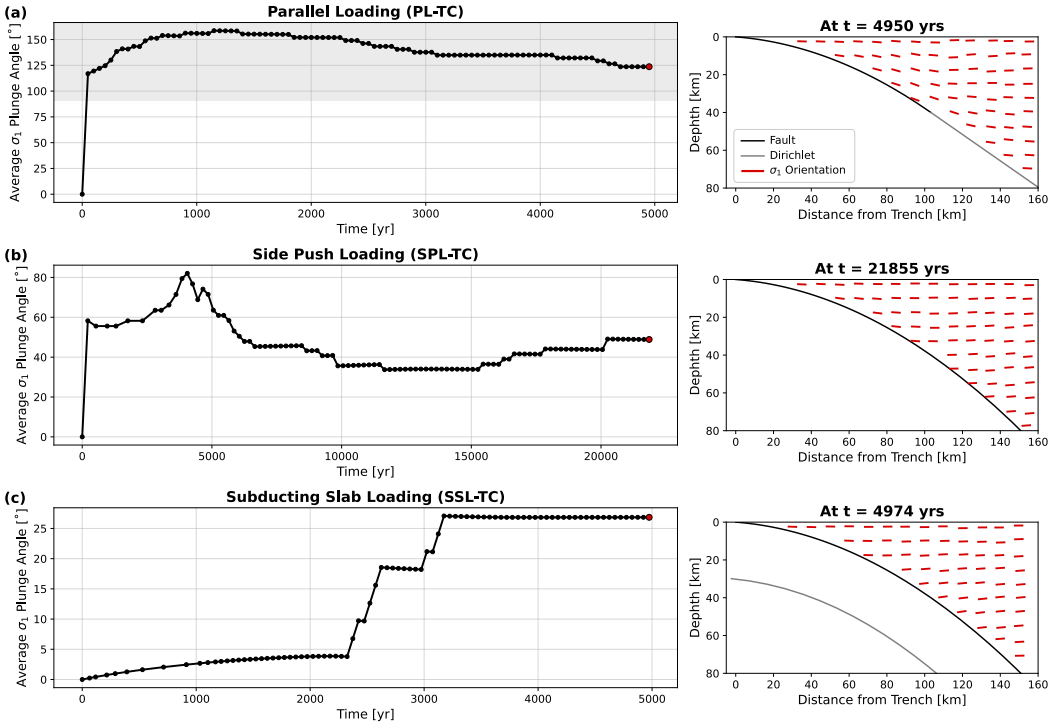

Figure 10. Spatially averaged plunge angle of the maximum compressive principal stress (σ_1) for uniform $\boldsymbol{\sigma}^B$ models (a) PL-TC, (b) SPL-TC, and (c) SSL-TC. (Left column) Evolution of the σ_1 plunge angle over time. The σ_1 plunge angle is measured counterclockwise from the vector $(-1, 0)$, such that values greater than 90° (grey shaded area) indicate plunge away from the slab interface and vice versa. The red point indicates the time at which the panels in the right columns are shown. (Right column) Spatial pattern of σ_1 orientations at final simulation time in each model (red), fault geometry (black), and interface governed by Dirichlet boundary condition (grey).

6.4 Which Loading Scheme Should We Use?

Based on comparisons of rupture characteristics and off-fault deformation patterns, we summarize the strengths and weaknesses of each loading scheme as follows. Parallel loading, when implemented with a planar fault, is conceptually analogous to the traditional backslip approach (Savage & Prescott, 1978; Savage, 1983), and produces earthquake cycles comparable to other software using boundary methods (e.g., Erickson et al., 2023). However, this loading scheme produces permanent surface displacements that accrue over time, inconsistent with geodetic (e.g., Bürgmann & Chadwell, 2014; Hamling et al., 2022; K. Wang & Tréhu, 2016) and geologic (e.g., Baker et al., 2013; Wesson et al., 2015) data. Significant stress accumulation, comparable to the coseismic stress drop, adds spurious complexity to the rupture characteristics, thereby challenging their reliability.

Side push loading has the virtue of simplicity, as it is independent of assumed fault geometry. However, the side push loading accumulates permanent vertical displacement, which challenges first-order comparisons with geodetic measurements. Although this loading scheme yields lower on-fault stressing rates than parallel loading, it still imposes non-negligible stress accumulation of a fraction of the coseismic stress drop, warranting caution when assessing rupture properties.

The numerical experiments show that the subducting slab loading, as it is consistent with the kinematic motion observed in subduction zones, accumulates little permanent strain in the overriding plate, and yields minimal cumulative stressing rates on the fault. Owing to small long-term surface displacement, this loading scheme facilitates a first-order comparison with geodetic records and makes subtle signals, such as those due to afterslip and SSEs, stand out more clearly. Since the loading method is sensitive to slab thickness, caution should be exercised during model design.

Our results highlight that different loading methods produce 1-2 orders of magnitude variation in modeled deformation patterns, particularly the long-term surface displacement accumulation (Figs. 4 & 5) and the on-fault stressing rate (Fig. 9). As illustrated by the three loading schemes explored here, we expect other types of loading methods to have their own virtues and limitations. Thus, we suggest future studies using SEAS models should carefully investigate and quantify the effect of the loading method on the study's target phenomena before interpreting the model results and comparing them with observational data.

We note that the models presented in this study assumed a linear elastic constitutive behavior in the bulk. In natural subduction zones, inelastic processes, such as viscoelasticity (e.g., Allison & Dunham, 2018; Luo et al., 2025; K. Wang et al., 2012), poroelasticity (Ozawa et al., 2024; Saffer & Tobin, 2011), and off-fault plasticity (e.g., Baker et al., 2013; Dunham et al., 2011; Erickson et al., 2017; Templeton & Rice, 2008; van Dinther et al., 2014), play important roles in producing observed surface deformation patterns or rupture characteristics. Without these processes, all three loading schemes cannot capture realistic deformation signals (Jolivet et al., 2020; Sun & Davis, 2026) and accumulate significant bending stress when the fault has varying curvature. However, under the widely accepted elasticity assumption, the suggested subducting slab loading captures first-order features of subduction zones.

7 Conclusions

We explore the effects of boundary conditions on rupture characteristics and off-fault deformation patterns in subduction zone SEAS simulations using volume-discretized methods. We compare "parallel", "side push", and "subducting slab" loading schemes that have been utilized in previous SEAS simulations or suggested by kinematic dislocation studies.

Earthquake characteristics, such as recurrence interval, slip per earthquake, static stress drop, and rupture length, are comparable between parallel and side push loading schemes, while additional sub-cycles different partial rupture earthquakes emerge in the subducting slab loading. Among the rupture characteristics, the maximum recurrence interval exhibits the most variability across the three loading methods. Our fully creeping fault models (category "C" models) demonstrate that parallel loading produces on-fault stressing rates on the order of kPa/yr, comparable to earthquake stress drops when accumulated over thousands of years. Side push and subducting slab loading schemes reduce these rates by 1-2 orders of magnitude. While these rates remain constant across the simulation for parallel and side push loading schemes, they diminish over time under subducting slab loading. These loading-related stress artifacts may inhibit convergence toward a steady-state earthquake sequence.

We find that the loading scheme can alter the magnitude and/or spatial pattern of strain rates, surface displacement, and principal stress. The strain rates within the domain are concentrated near the bottom of the fault and within the slab in parallel and subducting slab loading schemes, respectively, whereas they are relatively evenly distributed across the computational domain in side push loading. Side push and subducting slab loading schemes produce maximum compressive principal stress plunging at $\sim 25{-}50°$ towards the slab, while parallel loading produces those plunging sub-parallel to the slab. Parallel and side push loading schemes result in permanent long-term surface displacements, while subduction slab loading suppresses them by an order of magnitude after a few cycles.

Observed differences among the three loading schemes may depend on the size of the domain, such as the domain length in the side push loading and the slab thickness in the subducting slab loading. The domain length in the side push loading has a minimal impact on the rupture characteristics, mainly affecting the recurrence interval. Slab thickness in the subducting slab loading exhibits strong control on both on- and off-fault deformations, raising caution when designing the model.

The systematic comparison of three commonly used loading schemes in volumetric SEAS simulations demonstrates a significant impact of the loading method on observed rupture characteristics and deformation patterns. Our study suggests that subducting slab loading is consistent with geodetic and seismologically derived stress constraints in modeling 2D subduction zone earthquake cycles. We encourage practitioners using volumetric SEAS simulations to examine the influence of the implemented loading method using metrics such surface displacement and principal stress orientations, and assure they are consistent with observational data.

Open Research Section

All input data required for reproducing all models are available in the Zenodo repository (Yun et al., 2026). All simulations were conducted using the open-source software *Tandem* (Gabriel et al., 2025; Uphoff et al., 2023). An online documentation of *Tandem* is available at `https://tandem.readthedocs.io/en/latest/`. We use the dmay/seas-checkpoint branch (commit #1dc36db) for all simulations shown in this study.

Conflict of Interest declaration

The authors declare there are no conflicts of interest for this manuscript.

Acknowledgments

JY and AAG acknowledge generous support from Pacific Gas and Electric (PG&E). JY, DAM, and AAG acknowledge support from the National Science Foundation (QUAKE-

WORX, NSF grant number OAC-2311208) and the Statewide California Earthquake Center (SCEC award 25313). DAM and AAG acknowledge additional support from the National Science Foundation (NSF grants CAIG RISE-2531036, MTMOD EAR-2121568). AAG acknowledges additional support from the National Science Foundation (NSF grants CRESCENT EAR-2225286, LCCF-CSA OAC-2139536), and the National Aeronautics and Space Administration (NASA 80NSSC20K0495), as well as Horizon Europe (GeoINQUIRE, grant number 101058518 and ChEESE-2P, grant number 101093038). DL was partially funded by the National Science Foundation (NSF grant number EAR-2121666). CW was partially funded by the New Zealand Ministry of Business, Innovation and Employment (MBIE) through the Kaitiakitanga ki Te Riu-a-Māui (KTRM) Programme (Strategic Science Investment Fund, contract C05X1702). We gratefully acknowledge the computing resources provided by the Institute of Geophysics of LMU Munich (Oeser et al., 2006). We also acknowledge computing resources on Frontera (project EAR25002), provided by the Texas Advanced Computing Center (`https://tacc.utexas.edu/`).

References

Abhyankar, S., Brown, J., Constantinescu, E., Ghosh, D., & Smith, B. F. (2014). *PETSc/TS: A modern scalable DAE/ODE solver library* (Preprint No. ANL/MCS-P5061-0114). Argonne National Laboratory.

Allison, K. L., & Dunham, E. M. (2018). Earthquake cycle simulations with rate-and-state friction and power-law viscoelasticity. *Tectonophysics*, *733*, 232–256.

Ando, R., & Kaneko, Y. (2018). Dynamic rupture simulation reproduces spontaneous multifault rupture and arrest during the 2016 Mw 7.9 Kaikoura earthquake. *Geophysical Research Letters*, *45*(23), 12–875.

Asano, Y., Saito, T., Ito, Y., Shiomi, K., Hirose, H., Matsumoto, T., ... Sekiguchi, S. (2011). Spatial distribution and focal mechanisms of aftershocks of the 2011 off the Pacific coast of Tohoku Earthquake. *Earth, planets and space*, *63*(7), 669–673.

Baker, A., Allmendinger, R., Owen, L., & Rech, J. (2013). Permanent deformation caused by subduction earthquakes in northern Chile. *Nature Geoscience*, *6*(6), 492–496.

Balay, S., Abhyankar, S., Adams, M. F., Brown, J., Brune, P., Buschelman, K., ... Zhang, H. (2019). *PETSc users manual* (Tech. Rep. No. ANL-95/11 - Revision 3.11). Argonne National Laboratory.

Balay, S., Gropp, W. D., McInnes, L. C., & Smith, B. F. (1997). Efficient management of parallelism in object oriented numerical software libraries. In E. Arge, A. M. Bruaset, & H. P. Langtangen (Eds.), *Modern software tools in scientific computing* (pp. 163–202). Birkhäuser Press.

Barbot, S., Lapusta, N., & Avouac, J.-P. (2012). Under the hood of the earthquake machine: Toward predictive modeling of the seismic cycle. *Science*, *336*(6082), 707–710.

Biemiller, J., Gabriel, A.-A., May, D., & Staisch, L. (2024). Subduction zone geometry modulates the megathrust earthquake cycle: magnitude, recurrence, and variability. *Journal of Geophysical Research: Solid Earth*, *129*(8), e2024JB029191.

Bürgmann, R., & Chadwell, D. (2014). Seafloor geodesy. *Annual Review of Earth and Planetary Sciences*, *42*, 509–534.

Day, S. M. (1982). Three-dimensional simulation of spontaneous rupture: the effect of nonuniform prestress. *Bulletin of the Seismological Society of America*, *72*(6A), 1881–1902.

Dieterich, J. H. (1979). Modeling of rock friction: 1. Experimental results and constitutive equations. *Journal of Geophysical Research: Solid Earth*, *84*(B5), 2161–2168.

Duan, B. (2012). Dynamic rupture of the 2011 Mw 9.0 Tohoku-Oki earthquake:

Roles of a possible subducting seamount. *Journal of Geophysical Research: Solid Earth*, *117*(B5), B05311.

Duan, B., & Oglesby, D. D. (2006). Heterogeneous fault stresses from previous earthquakes and the effect on dynamics of parallel strike-slip faults. *Journal of Geophysical Research: Solid Earth*, *111*(B5).

Dunham, E. M., Belanger, D., Cong, L., & Kozdon, J. E. (2011). Earthquake ruptures with strongly rate-weakening friction and off-fault plasticity, part 2: Nonplanar faults. *Bulletin of the Seismological Society of America*, *101*(5), 2308–2322.

England, P. C., & May, D. A. (2021). The global range of temperatures on convergent plate interfaces. *Geochemistry, Geophysics, Geosystems*, *22*(8), e2021GC009849.

Erickson, B. A., & Dunham, E. M. (2014). An efficient numerical method for earthquake cycles in heterogeneous media: Alternating subbasin and surface-rupturing events on faults crossing a sedimentary basin. *Journal of Geophysical Research: Solid Earth*, *119*(4), 3290–3316.

Erickson, B. A., Dunham, E. M., & Khosravifar, A. (2017). A finite difference method for off-fault plasticity throughout the earthquake cycle. *Journal of the Mechanics and Physics of Solids*, *109*, 50–77.

Erickson, B. A., Jiang, J., Barall, M., Lapusta, N., Dunham, E. M., Harris, R., ... others (2020). The community code verification exercise for simulating sequences of earthquakes and aseismic slip (SEAS). *Seismological Research Letters*, *91*(2A), 874–890.

Erickson, B. A., Jiang, J., Lambert, V., Barbot, S. D., Abdelmeguid, M., Almquist, M., ... others (2023). Incorporating full elastodynamic effects and dipping fault geometries in community code verification exercises for simulations of earthquake sequences and aseismic slip (SEAS). *Bulletin of the Seismological Society of America*, *113*(2), 499–523.

Gabriel, A.-A., Karki, P., Magen, Y., Oryan, B., Ulrich, T., Yun, J., & May, D. A. (2025). Tandem: An Open-Source High-Performance Computing Volumetric Software to Model Sequences of Earthquakes and Aseismic Slip Across Complex Fault Systems.

Glehman, J., Gabriel, A., Ulrich, T., Ramos, M., Huang, Y., & Lindsey, E. (2025). Partial ruptures governed by the complex interplay between geodetic slip deficit, rigidity, and pore fluid pressure in 3D Cascadia dynamic rupture simulations. *Seismica*, *2*(4). doi: 10.26443/seismica.v2i4.1427

Govers, R., Furlong, K., Van de Wiel, L., Herman, M., & Broerse, T. (2018). The geodetic signature of the earthquake cycle at subduction zones: Model constraints on the deep processes. *Reviews of Geophysics*, *56*(1), 6–49.

Hamling, I. J., Wright, T. J., Hreinsdóttir, S., & Wallace, L. M. (2022). A snapshot of New Zealand's dynamic deformation field from Envisat InSAR and GNSS observations between 2003 and 2011. *Geophysical Research Letters*, *49*(2), e2021GL096465.

Hansen, S., & Schmandt, B. (2017). P and S wave receiver function imaging of subduction with scattering kernels. *Geochemistry, Geophysics, Geosystems*, *18*(12), 4487–4502.

Hardebeck, J. L. (2012). Coseismic and postseismic stress rotations due to great subduction zone earthquakes. *Geophysical Research Letters*, *39*(21), L21313.

Hardebeck, J. L. (2015). Stress orientations in subduction zones and the strength of subduction megathrust faults. *Science*, *349*(6253), 1213–1216.

Harris, R. A., & Day, S. M. (1999). Dynamic 3D simulations of earthquakes on en echelon faults. *Geophysical Research Letters*, *26*(14), 2089–2092.

Hasegawa, A., Yoshida, K., Asano, Y., Okada, T., Iinuma, T., & Ito, Y. (2012). Change in stress field after the 2011 great tohoku-oki earthquake. *Earth and Planetary Science Letters*, *355*, 231–243.

Hasegawa, A., Yoshida, K., & Okada, T. (2011). Nearly complete stress drop in the 2011 M w 9.0 off the Pacific coast of Tohoku Earthquake. *Earth, planets and space*, *63*(7), 35.

Herrera, M. T., Crempien, J. G., Cembrano, J., & Moreno, M. (2024). Seismic cycle controlled by subduction geometry: novel 3-D quasi-dynamic model of Central Chile megathrust. *Geophysical Journal International*, *237*(2), 772–787.

Hill, E. M., Borrero, J. C., Huang, Z., Qiu, Q., Banerjee, P., Natawidjaja, D. H., ... others (2012). The 2010 Mw 7.8 Mentawai earthquake: Very shallow source of a rare tsunami earthquake determined from tsunami field survey and near-field GPS data. *Journal of Geophysical Research: Solid Earth*, *117*(B6).

Hillers, G., Ben-Zion, Y., & Mai, P. M. (2006). Seismicity on a fault controlled by rate-and state-dependent friction with spatial variations of the critical slip distance. *Journal of Geophysical Research: Solid Earth*, *111*(B1).

Ito, Y., Hino, R., Kido, M., Fujimoto, H., Osada, Y., Inazu, D., ... others (2013). Episodic slow slip events in the Japan subduction zone before the 2011 Tohoku-Oki earthquake. *Tectonophysics*, *600*, 14–26.

Jiang, J., Erickson, B. A., Lambert, V. R., Ampuero, J.-P., Ando, R., Barbot, S. D., ... others (2022). Community-driven code comparisons for three-dimensional dynamic modeling of sequences of earthquakes and aseismic slip. *Journal of Geophysical Research: Solid Earth*, *127*(3), e2021JB023519.

Jiang, J., & Lapusta, N. (2016). Deeper penetration of large earthquakes on seismically quiescent faults. *Science*, *352*(6291), 1293–1297.

Jolivet, R., & Frank, W. (2020). The transient and intermittent nature of slow slip. *AGU Advances*, *1*(1), e2019AV000126.

Jolivet, R., Simons, M., Duputel, Z., Olive, J.-A., Bhat, H., & Bletery, Q. (2020). Interseismic loading of subduction megathrust drives long-term uplift in northern Chile. *Geophysical Research Letters*, *47*(8), e2019GL085377.

Kanda, R. V., & Simons, M. (2010). An elastic plate model for interseismic deformation in subduction zones. *Journal of Geophysical Research: Solid Earth*, *115*(B3), B03405.

Kaneko, Y., Ampuero, J.-P., & Lapusta, N. (2011). Spectral-element simulations of long-term fault slip: Effect of low-rigidity layers on earthquake-cycle dynamics. *Journal of Geophysical Research: Solid Earth*, *116*(B10), B10313.

Kato, A., Obara, K., Igarashi, T., Tsuruoka, H., Nakagawa, S., & Hirata, N. (2012). Propagation of slow slip leading up to the 2011 M w 9.0 Tohoku-Oki earthquake. *Science*, *335*(6069), 705–708.

Kozdon, J. E., Dunham, E. M., & Nordström, J. (2013). Simulation of dynamic earthquake ruptures in complex geometries using high-order finite difference methods. *Journal of Scientific Computing*, *55*(1), 92–124.

Lambert, V. R., Erickson, B. A., Jiang, J., Dunham, E. M., Kim, T., Ampuero, J.-P., ... others (2025). Community-driven code comparisons for simulations of fluid-induced aseismic slip. *Journal of Geophysical Research: Solid Earth*, *130*(4), e2024JB030601.

Lapusta, N., & Liu, Y. (2009). Three-dimensional boundary integral modeling of spontaneous earthquake sequences and aseismic slip. *Journal of Geophysical Research: Solid Earth*, *114*(B9).

Lapusta, N., Rice, J. R., Ben-Zion, Y., & Zheng, G. (2000). Elastodynamic analysis for slow tectonic loading with spontaneous rupture episodes on faults with rate-and state-dependent friction. *Journal of Geophysical Research: Solid Earth*, *105*(B10), 23765–23789.

Li, D., & Gabriel, A.-A. (2024). Linking 3D long-term slow-slip cycle models with rupture dynamics: The nucleation of the 2014 M_w 7.3 Guerrero, Mexico earthquake. *AGU Advances*, *5*(2), e2023AV000979.

Li, D., & Liu, Y. (2016). Spatiotemporal evolution of slow slip events in a nonplanar fault model for northern Cascadia subduction zone. *Journal of Geophysical Re-*

search: Solid Earth, *121*(9), 6828–6845.

Li, M., Pranger, C., & van Dinther, Y. (2022). Characteristics of earthquake cycles: A cross-dimensional comparison of 0D to 3D numerical models. *Journal of Geophysical Research: Solid Earth*, *127*(8), e2021JB023726.

Lindsey, E. O., Mallick, R., Hubbard, J. A., Bradley, K. E., Almeida, R. V., Moore, J. D., ... Hill, E. M. (2021). Slip rate deficit and earthquake potential on shallow megathrusts. *Nature Geoscience*, *14*(5), 321–326.

Liu, D., Duan, B., & Luo, B. (2020). EQsimu: a 3-D finite element dynamic earthquake simulator for multicycle dynamics of geometrically complex faults governed by rate-and state-dependent friction. *Geophysical Journal International*, *220*(1), 598–609.

Luo, H., Wang, K., Feng, L., & Hill, E. M. (2025). Interseismic secondary zone of subsidence during earthquake cycles in subduction zones. *Nature Geoscience*, *18*(10), 1027–1033.

Ma, S., & Hirakawa, E. T. (2013). Dynamic wedge failure reveals anomalous energy radiation of shallow subduction earthquakes. *Earth and Planetary Science Letters*, *375*, 113–122.

Madden, E. H., Ulrich, T., & Gabriel, A.-A. (2022). The state of pore fluid pressure and 3-D megathrust earthquake dynamics. *Journal of Geophysical Research: Solid Earth*, *127*(4), e2021JB023382.

Meng, Q., & Duan, B. (2023). Dynamic modeling of interactions between shallow slow-slip events and subduction earthquakes. *Seismological Society of America*, *94*(1), 206–216.

Mia, M. S., Abdelmeguid, M., Harris, R. A., & Elbanna, A. E. (2024). Rupture jumping and seismic complexity in models of earthquake cycles for fault stepovers with off-fault plasticity. *Bulletin of the Seismological Society of America*, *114*(3), 1466–1480.

Molina-Ormazabal, D., Ampuero, J.-P., & Tassara, A. (2023). Diverse slip behaviour of velocity-weakening fault barriers. *Nature Geoscience*, *16*(12), 1200–1207.

Morris, A., Ferrill, D. A., & Henderson, D. B. (1996). Slip-tendency analysis and fault reactivation. *Geology*, *24*(3), 275–278.

Noda, H., Lapusta, N., & Kanamori, H. (2013). Comparison of average stress drop measures for ruptures with heterogeneous stress change and implications for earthquake physics. *Geophysical Journal International*, *193*(3), 1691–1712.

Oeser, J., Bunge, H.-P., & Mohr, M. (2006). Cluster design in the earth sciences tethys. In *International conference on high performance computing and communications* (pp. 31–40).

Ozawa, S., & Ando, R. (2021). Mainshock and aftershock sequence simulation in geometrically complex fault zones. *Journal of Geophysical Research: Solid Earth*, *126*(2), e2020JB020865.

Ozawa, S., Yang, Y., & Dunham, E. M. (2024). Fault-valve instability: A mechanism for slow slip events. *Journal of Geophysical Research: Solid Earth*, *129*(10), e2024JB029165.

Pardo, M., Comte, D., & Monfret, T. (2002). Seismotectonic and stress distribution in the central Chile subduction zone. *Journal of South American Earth Sciences*, *15*(1), 11–22.

Perez-Silva, A., Kaneko, Y., Savage, M., Wallace, L., Li, D., & Williams, C. (2022). Segmentation of Shallow Slow Slip Events at the Hikurangi Subduction Zone Explained by Along-Strike Changes in Fault Geometry and Plate Convergence Rates. *Journal of Geophysical Research: Solid Earth*, *127*(1), e2021JB022913.

Pranger, C., Sanan, P., May, D. A., Le Pourhiet, L., & Gabriel, A.-A. (2022). Rate and state friction as a spatially regularized transient viscous flow law. *Journal of Geophysical Research: Solid Earth*, *127*(6), e2021JB023511.

Pranger, C. C. (2020). *Unstable physical processes operating on self-governing fault systems, improved modeling methodology* (Unpublished doctoral dissertation).

tured curvilinear grids. *Geophysical Journal International*, *233*(1), 586–626.
van Dinther, Y., Mai, P. M., Dalguer, L. A., & Gerya, T. (2014). Modeling the seismic cycle in subduction zones: The role and spatiotemporal occurrence of off-megathrust earthquakes. *Geophysical Research Letters*, *41*(4), 1194–1201.
Walcott, R. (1970). Flexural rigidity, thickness, and viscosity of the lithosphere. *Journal of Geophysical Research*, *75*(20), 3941–3954.
Wallace, L. M., Webb, S. C., Ito, Y., Mochizuki, K., Hino, R., Henrys, S., ... Sheehan, A. F. (2016). Slow slip near the trench at the Hikurangi subduction zone, New Zealand. *Science*, *352*(6286), 701–704.
Wang, K., Hu, Y., & He, J. (2012). Deformation cycles of subduction earthquakes in a viscoelastic Earth. *Nature*, *484*(7394), 327–332.
Wang, K., & Tréhu, A. M. (2016). Invited review paper: Some outstanding issues in the study of great megathrust earthquakes—The Cascadia example. *Journal of Geodynamics*, *98*, 1–18.
Wang, S. (2024). Toward quantitative characterization of simulated earthquake-cycle complexities. *Scientific Reports*, *14*(1), 16811.
Weng, H., & Yang, H. (2018). Constraining frictional properties on fault by dynamic rupture simulations and near-field observations. *Journal of Geophysical Research: Solid Earth*, *123*(8), 6658–6670.
Wesson, R. L., Melnick, D., Cisternas, M., Moreno, M., & Ely, L. L. (2015). Vertical deformation through a complete seismic cycle at isla santa maría, chile. *Nature Geoscience*, *8*(7), 547–551.
Williams, C. A., Eberhart-Phillips, D., Bannister, S., Barker, D. H., Henrys, S., Reyners, M., & Sutherland, R. (2013). Revised interface geometry for the Hikurangi subduction zone, New Zealand. *Seismological Research Letters*, *84*(6), 1066–1073.
Wong, J. W. C., Gabriel, A.-A., & Fan, W. (2026). Dynamic restrengthening and fault heterogeneity explain megathrust earthquake complexity. *Nature Communications*.
Woods, K., Wallace, L. M., Williams, C. A., Hamling, I. J., Webb, S. C., Ito, Y., ... others (2024). Spatiotemporal evolution of slow slip events at the offshore Hikurangi Subduction Zone in 2019 using GNSS, InSAR, and seafloor geodetic data. *Journal of Geophysical Research: Solid Earth*, *129*(8), e2024JB029068.
Yokota, Y., Ishikawa, T., & Watanabe, S.-i. (2018). Seafloor crustal deformation data along the subduction zones around Japan obtained by GNSS-A observations. *Scientific data*, *5*(1), 180182.
Yu, H., Liu, Y., Yang, H., & Ning, J. (2018). Modeling earthquake sequences along the Manila subduction zone: Effects of three-dimensional fault geometry. *Tectonophysics*, *733*, 73–84.
Yun, J., Fialko, Y., May, D. A., Gabriel, A.-A., Williams, C., & Liu, D. (2026). *Supplementary material for "Effects of loading schemes in volumetric simulations of sequences of earthquakes and aseismic slip (SEAS) in subduction zones".* (Version v1) [Dataset]. Zenodo. Retrieved from `https://tinyurl.com/yvyxnybh` doi: https://doi.org/10.5281/zenodo.20387748
Yun, J., Gabriel, A.-A., May, D. A., & Fialko, Y. (2025). Effects of Stress and Friction Heterogeneity on Spatiotemporal Complexity of Seismic and Aseismic Slip on Strike-Slip Faults. *Journal of Geophysical Research: Solid Earth*, *130*(12), e2025JB031270. doi: https://doi.org/10.1029/2025JB031270
Zhan, Z., Helmberger, D., Simons, M., Kanamori, H., Wu, W., Cubas, N., ... others (2012). Anomalously steep dips of earthquakes in the 2011 Tohoku-Oki source region and possible explanations. *Earth and Planetary Science Letters*, *353*, 121–133.

ETH Zurich.

Ramos, M. D., Thakur, P., Huang, Y., Harris, R. A., & Ryan, K. J. (2022). Working with dynamic earthquake rupture models: A practical guide. *Seismological Society of America*, *93*(4), 2096–2110.

Rice, J. R. (1993). Spatio-temporal complexity of slip on a fault. *Journal of Geophysical Research: Solid Earth*, *98*(B6), 9885–9907.

Rodriguez Piceda, C., Mildon, Z. K., Andrews, B. J., Yin, Y., Ampuero, J.-P., van den Ende, M., ... Galvez, P. (2026). The role of fault network geometry on the complexity of seismic cycles in the Apennines. *Solid Earth*, *17*(2), 311–346.

Romanet, P., Bhat, H. S., Jolivet, R., & Madariaga, R. (2018). Fast and slow slip events emerge due to fault geometrical complexity. *Geophysical Research Letters*, *45*(10), 4809–4819.

Ruina, A. (1983). Slip instability and state variable friction laws. *Journal of Geophysical Research: Solid Earth*, *88*(B12), 10359–10370.

Saffer, D. M., & Tobin, H. J. (2011). Hydrogeology and mechanics of subduction zone forearcs: Fluid flow and pore pressure. *Annual Review of Earth and Planetary Sciences*, *39*(1), 157–186.

Savage, J. C. (1983). A dislocation model of strain accumulation and release at a subduction zone. *Journal of Geophysical Research: Solid Earth*, *88*(B6), 4984–4996.

Savage, J. C., & Prescott, W. (1978). Asthenosphere readjustment and the earthquake cycle. *Journal of Geophysical Research: Solid Earth*, *83*(B7), 3369–3376.

Shibazaki, B., Wallace, L. M., Kaneko, Y., Hamling, I., Ito, Y., & Matsuzawa, T. (2019). Three-dimensional modeling of spontaneous and triggered slow-slip events at the Hikurangi subduction zone, New Zealand. *Journal of Geophysical Research: Solid Earth*, *124*(12), 13250–13268.

Shreedharan, S., Saffer, D., Wallace, L. M., & Williams, C. (2023). Ultralow frictional healing explains recurring slow slip events. *Science*, *379*(6633), 712–717.

Stein, S., & Okal, E. A. (2005). Speed and size of the Sumatra earthquake. *Nature*, *434*(7033), 581–582.

Sun, T., & Davis, E. E. (2026). Strain accumulation associated with locked subduction megathrusts revealed by deep-ocean borehole observations. *Science Advances*, *12*(16), eaea7133.

Takeuchi, C. S., & Fialko, Y. (2012). Dynamic models of interseismic deformation and stress transfer from plate motion to continental transform faults. *Journal of Geophysical Research: Solid Earth*, *117*(B5), B05403.

Tal, Y., & Gabrieli, T. (2024). Dual effect of roughness during earthquake rupture sequences on faults with strongly rate-weakening friction. *Earth and Planetary Science Letters*, *637*, 118738.

Templeton, E. L., & Rice, J. R. (2008). Off-fault plasticity and earthquake rupture dynamics: 1. Dry materials or neglect of fluid pressure changes. *Journal of Geophysical Research: Solid Earth*, *113*(B9).

Thakur, P., & Huang, Y. (2021). Influence of fault zone maturity on fully dynamic earthquake cycles. *Geophysical Research Letters*, *48*(17), e2021GL094679.

Trubienko, O., Fleitout, L., Garaud, J.-D., & Vigny, C. (2013). Interpretation of interseismic deformations and the seismic cycle associated with large subduction earthquakes. *Tectonophysics*, *589*, 126–141.

Ulrich, T., Gabriel, A.-A., Ampuero, J.-P., & Xu, W. (2019). Dynamic viability of the 2016 Mw 7.8 Kaikōura earthquake cascade on weak crustal faults. *Nature communications*, *10*(1), 1213.

Uphoff, C., May, D. A., & Gabriel, A.-A. (2023). A discontinuous Galerkin method for sequences of earthquakes and aseismic slip on multiple faults using unstruc-

Supplementary material for "Effects of loading schemes in volumetric simulations of sequences of earthquakes and aseismic slip (SEAS) in subduction zones"

Jeena Yun[1], Yuri Fialko[1], Dave A. May[1], Alice-Agnes Gabriel[1,2], Charles A. Williams[3], and Dunyu Liu[4]

[1]Scripps Institution of Oceanography, University of California San Diego, La Jolla, CA, USA

[2]Department of Earth and Environmental Sciences, Ludwig-Maximilians Universität München, Munich, Germany

[3]Earth Sciences New Zealand, Lower Hutt, New Zealand

[4]Institute for Geophysics, Jackson School of Geosciences, The University of Texas at Austin, TX, USA

Contents of this file

1. Text S1
2. Figures S1 to S13
3. Table S1

Additional Supporting Information (Files uploaded separately)

1. Movie S1

Corresponding author: Jeena Yun (j4yun@ucsd.edu)

Introduction

Text S1. Effects of slab thickness, domain length, and thickness of the far-field zero-displacement boundary in subducting slab loading

Eq. (5) in the main text indicates that the deformation patterns using subduction slab loading may depend on three length scales: slab thickness (D), domain length (x_{end} in Eq. (5)), and thickness of the far-field zero-displacement boundary (y_f in Eq. (5)). The base setup for the subduction slab loading (model SSL) uses $D = 30$ km, $y_f = -30$ km, and $x_{end} =\sim 245$ km, while model SSL-L in the main text uses $D = 100$ km while keeping the other two values the same. To analyze how these length scales affect strain rate in the domain and surface displacement, we perform additional models: 1) $D = 100$ km, $y_f = -30$ km, and $x_{end} =\sim 245$ km (denoted model SM1 and SM1-C), 2) $D = 30$ km, $y_f = -30$ km, and $x_{end} = \sim 352$ km (denoted model SM2 and SM2-C), and 3) $D = 100$ km, $y_f = -100$ km, and $x_{end} =\sim 352$ km (denoted model SM3 and SM2-C). x_{end} of ~ 352 km results from an extended slab reaching a maximum depth of 400 km. See Table S1 for a detailed description of each model.

Figures S12 and S13 show that, among these three length scales, slab thickness is the most prominent factor in altering strain distribution within the domain and surface displacement patterns. Comparing models SSL-LC (Fig. S9b) and SM1 (Fig. S12a) shows that varying the y_f value has little effect on strain rate distribution within the domain, particularly near the slab. Increasing domain length, as illustrated by models SSL-C (Fig. S9c) and SM2 (Fig. S12b), introduces a localized increase in strain rate near 150-250 km depth range, but little change in the shallower part of the domain. Comparing models SM2 and SM3 (Figs. S12b-c) shows that an increase in slab thickness

yields accumulation of strong compressive strain near the slab and tensile strain near the surface, similar to the comparison between models SSL-C and SSL-LC with a smaller x_{end} (see Section 6.1 in the main text). Similarly, changing the D value yields more distinctive interseismic surface velocities than changing y_f or x_{end} values (Fig. S13).

Movie S1.

Evolution of surface displacement during eight earthquakes since the spin-up phase, produced by (a) the parallel (model PL), (b) the side push (model SPL), and (c) the subducting slab (model SSL) loading schemes. All displacements are relative to a far-field station located at 245 km from the trench. For visual clarity, the arrow size is exaggerated, and its scale is shown in the bottom right corner. Triangles indicate the station locations that record synthetic displacements, and those colored in purple are the stations shown in Figure 5.

References

Hansen, S., & Schmandt, B. (2017). P and S wave receiver function imaging of subduction with scattering kernels. *Geochemistry, Geophysics, Geosystems*, *18*(12), 4487–4502.

Table S1. Descriptions of additional subducting slab loading models and the corresponding tags used in this study. D: slab thickness, x_{end}: domain length (Eq. (5)), y_f: thickness of the far-field zero-displacement boundary (Eq. (5)).

Model Tag	D [km]	y_f [km]	x_{end} [km]
SSL & SSL-C	30	-30	245
SSL-L & SSL-LC	100	-100	245
SM1 & SM1-C	100	-30	245
SM2 & SM2-C	30	-30	352
SM3 & SM3-C	100	-100	352

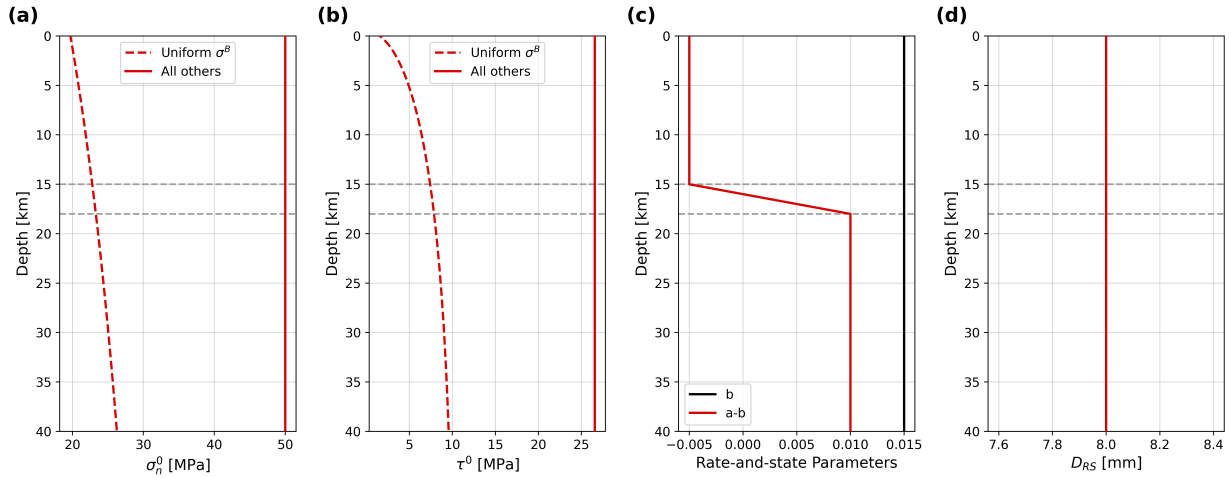

Figure S1. Input frictional parameters used in this study: (a) Effective normal stress, (b) initial shear stress, (c) rate-and-state parameters, and (d) characteristic state evolution distance. The dashed lines in panels (a-b) are the initial effective normal and shear stresses in uniform σ^B models.

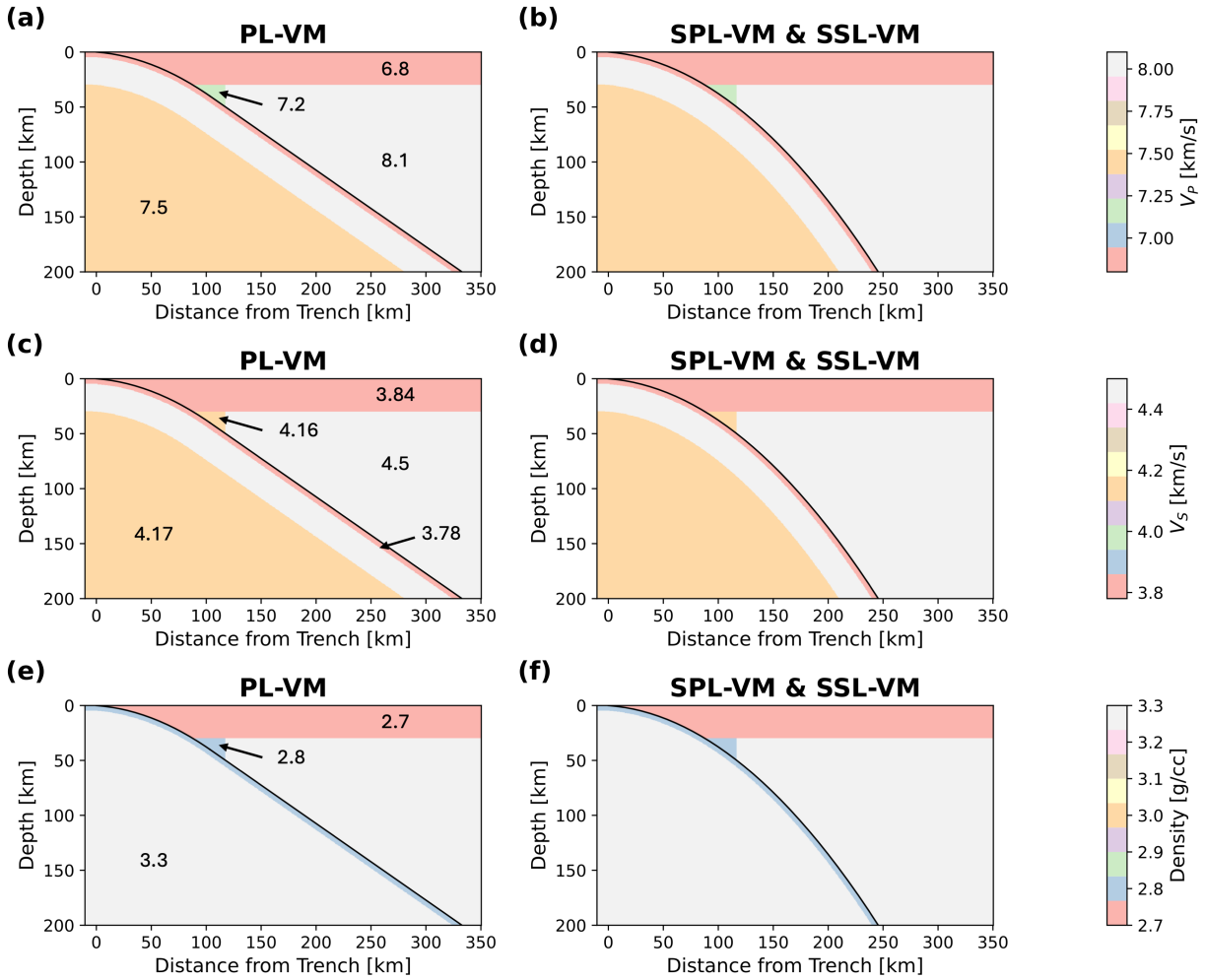

Figure S2. Spatially varying elastic parameters used in models PL-VM, SPL-VM, and SSL-VM, adopted from Hansen and Schmandt (2017). Note the slightly different distribution of the elastic parameters due to the difference in geometry between model PL-VM and the other two models.

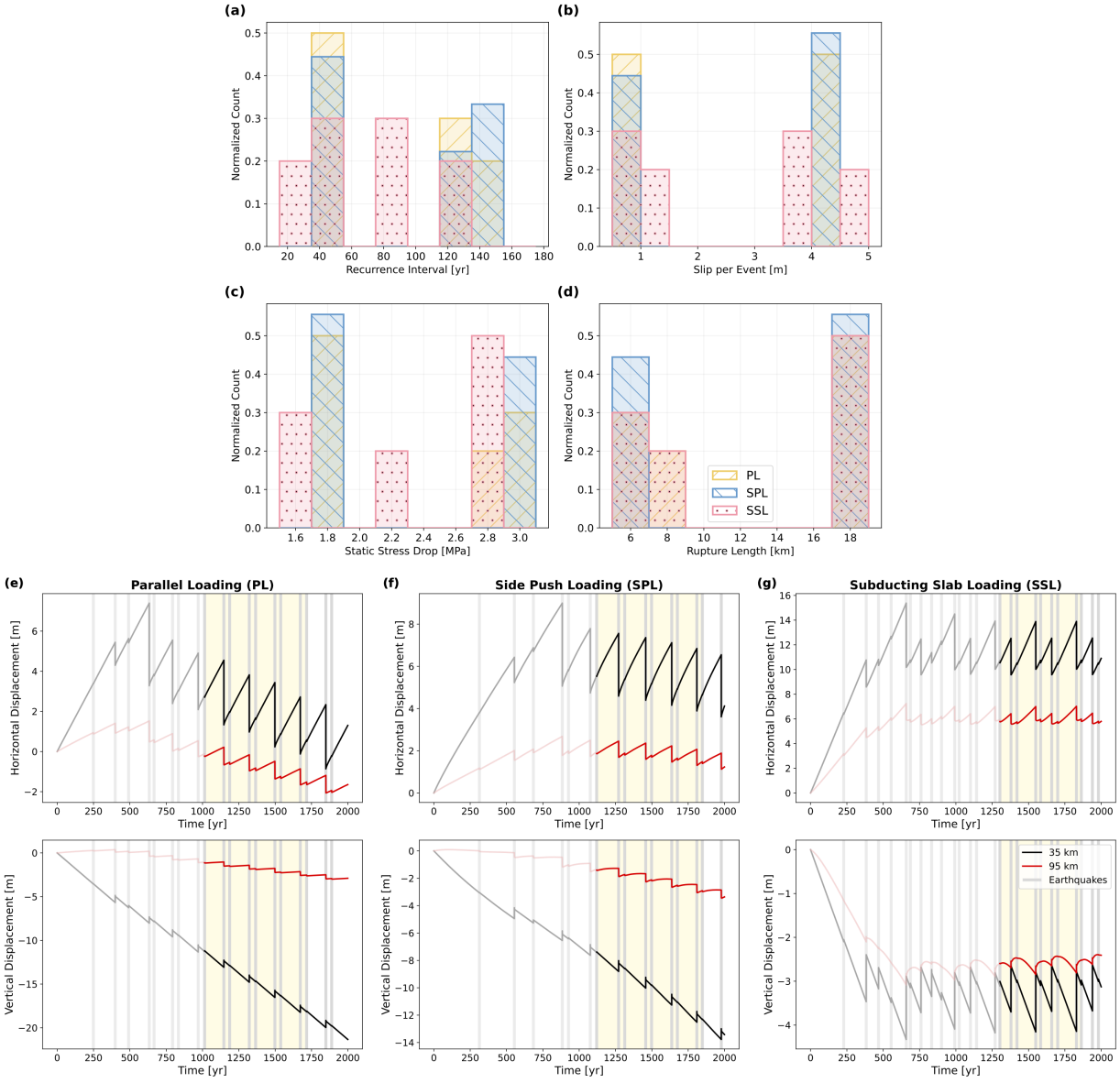

Figure S3. Earthquake characteristics (a-d) and surface displacements (e-g) for the three loading schemes, but using meshes with 2 times smaller on-fault element size. Compare panels (a-d) with Figure3 in the main text and panels (e-g) with Figure 5 in the main text.

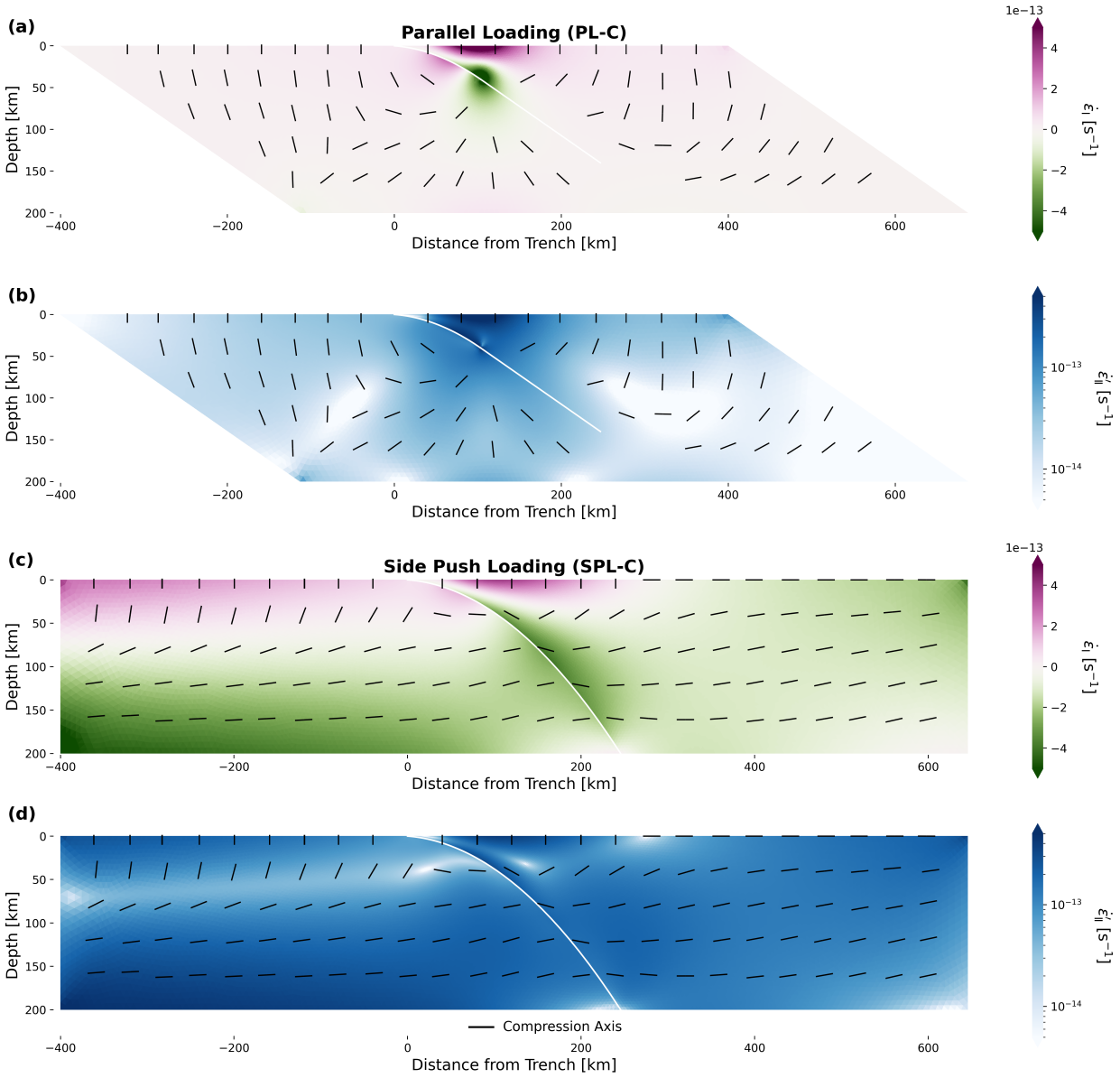

Figure S4. Invariants of strain rate tensors across the entire computational domain computed from (a-b) model PL-C and (c-d) model SPL-C. Panels (a) and (c) show the first invariant of the strain rate tensor and panels (b) and (d) show the second invariant of the deviatoric strain rate tensor. Color scales are the same as those used in Figure 8 in the main text.

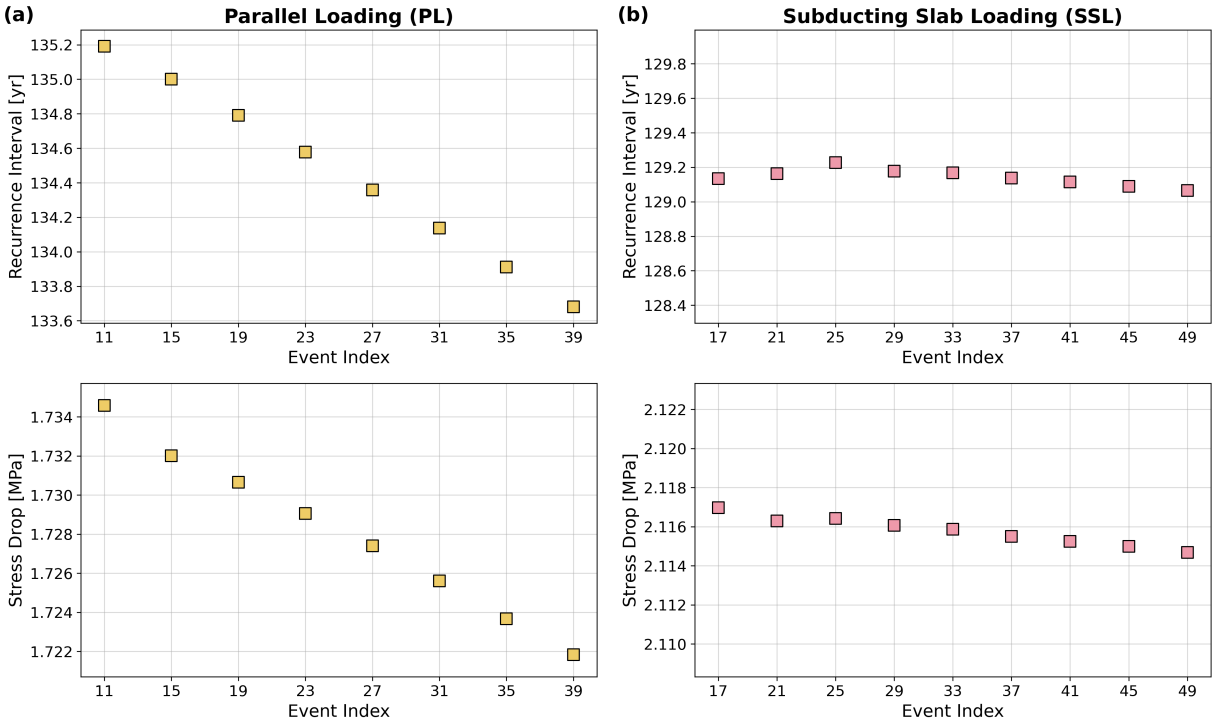

Figure S5. Evolution of the recurrence interval (top row) and stress drop (bottom row) of the 9 final system-size earthquakes in (a) parallel (model PL) and (b) subducting slab (model SSL) loadings. Since both models exhibit bimodal recurrence behavior, only every other system-size earthquake is plotted to show one group of the sequence more clearly. For direct comparison, the two models share the same y-axis range of 1.7 yrs for the recurrence interval and 0.015 MPa for the stress drop. Events 11 to 39 span 2450 yrs in model PL (panel a) and events 17 to 49 span 2240 yrs in model SSL (panel b).

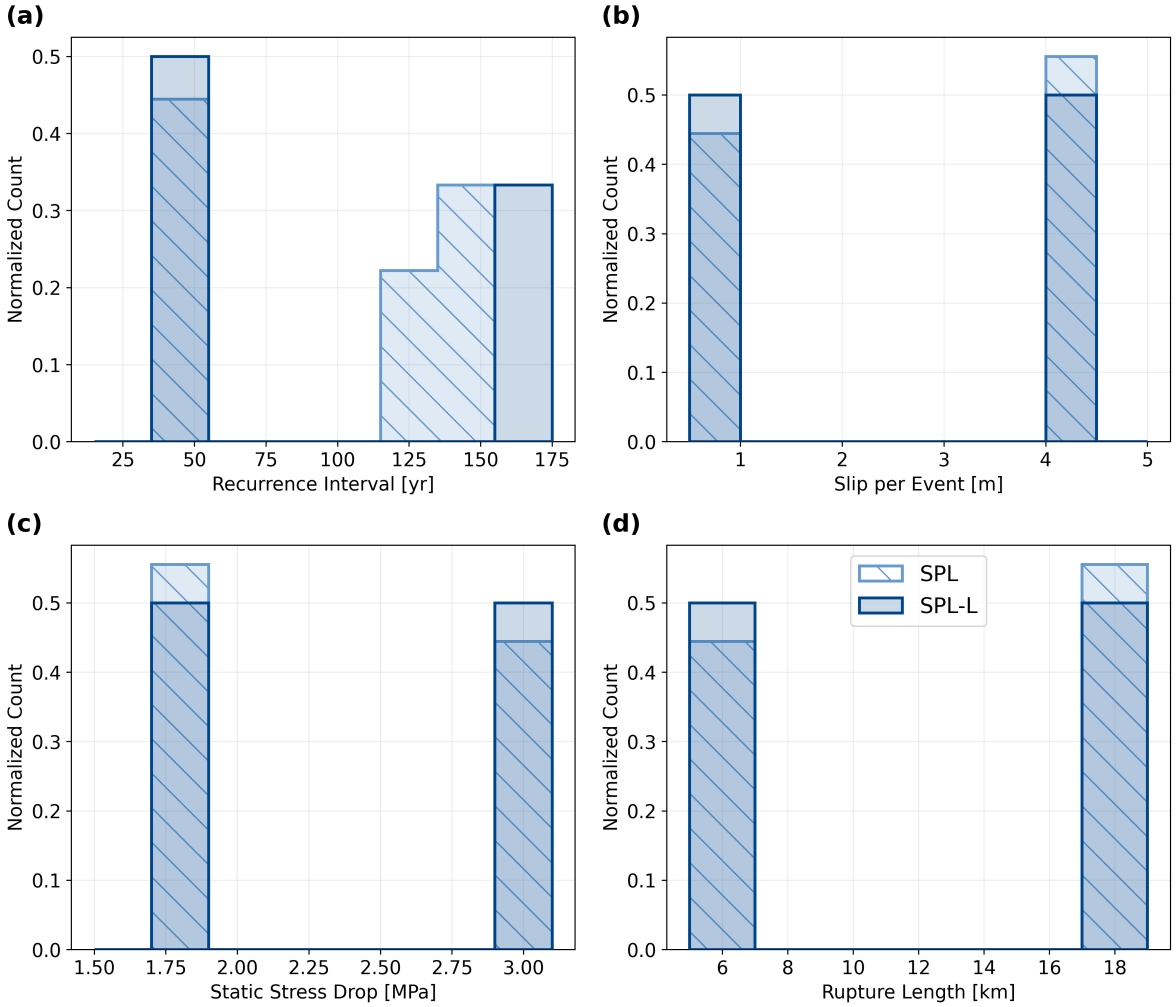

Figure S6. Same as Figure 3 in the main text, but for the side push loading schemes with two different computational domain widths: model SPL with 1,000 km width (light blue, hatched) and model SPL-L with 1,800 km width (dark blue).

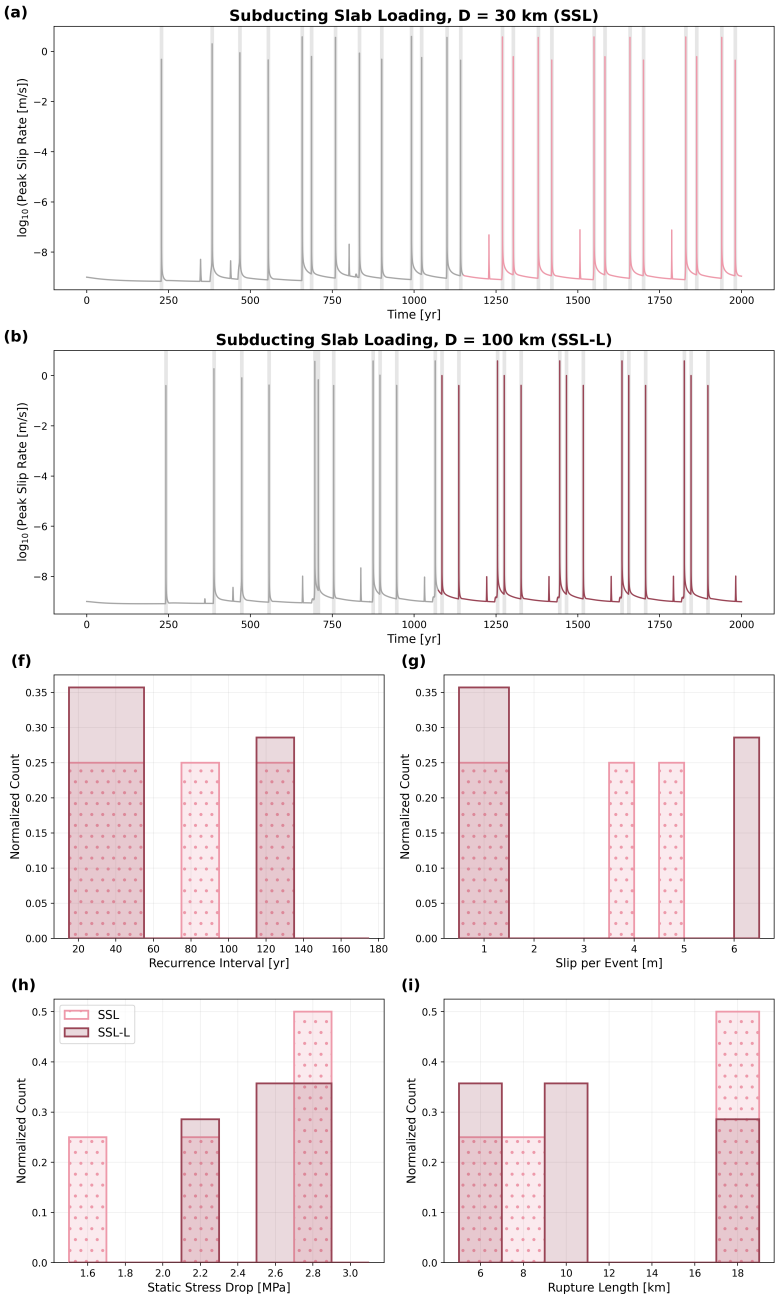

Figure S7. Same as Figure 3 in the main text, but for the subducting slab loading schemes with two different slab thickness values: model SSL with $D = 30$ km (pink) and model SSL-L with $D = 100$ km (brown).

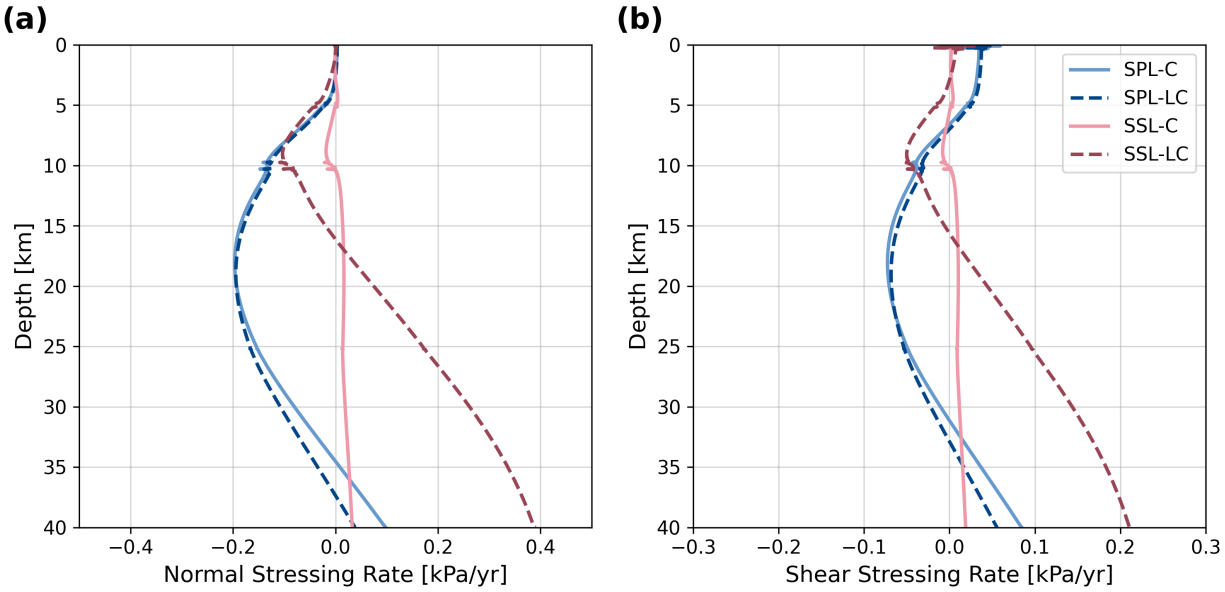

Figure S8. Stressing rates after 1,000 years of simulation for models SPL-C (light blue), SPL-L (blue dashed), SSL (pink), and SSL-L (brown dashed).

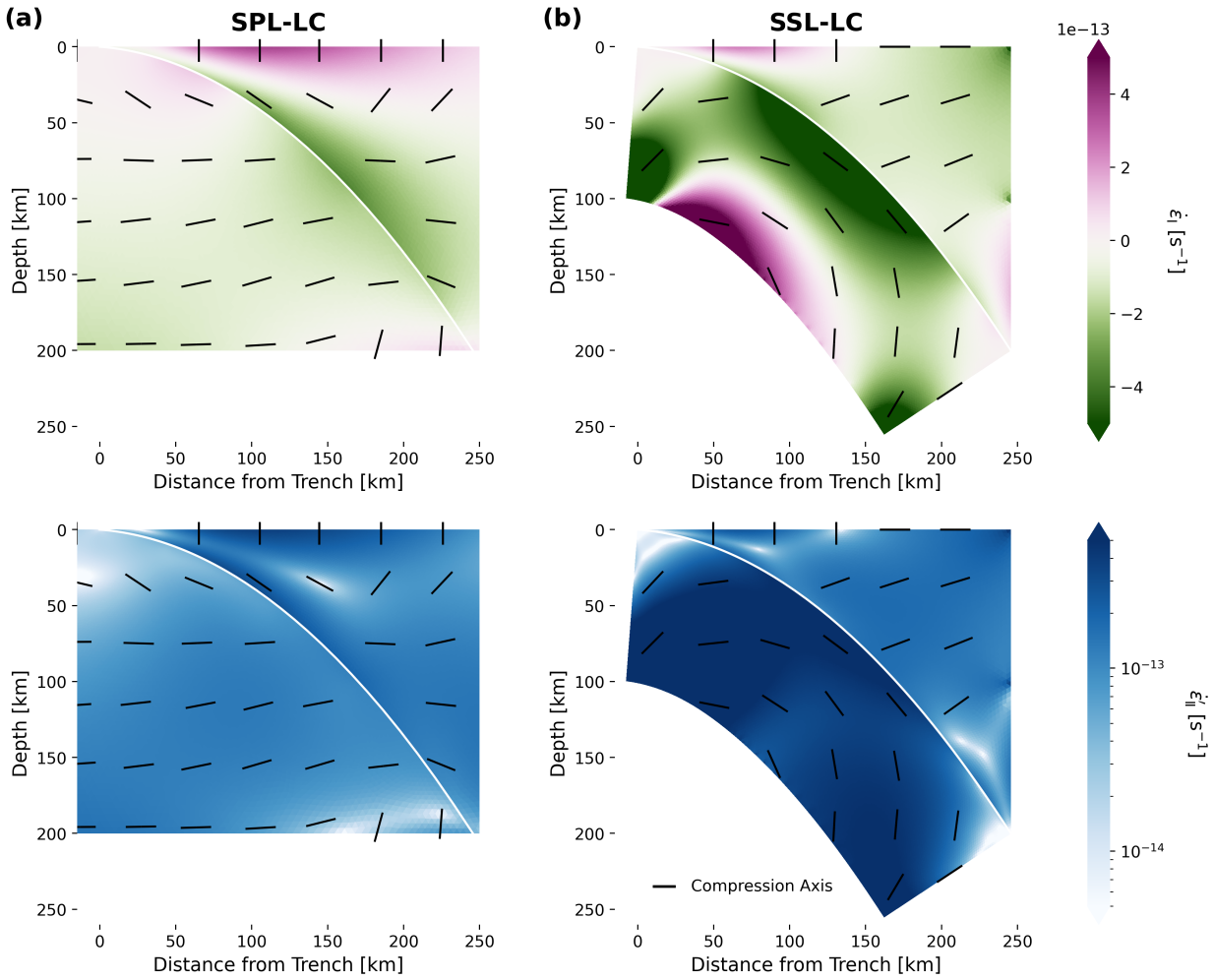

Figure S9. Same as Figure 8 in the main text, but for models SPL-LC and SSL-LC. Color scales are the same as those used in Figure 8 in the main text.

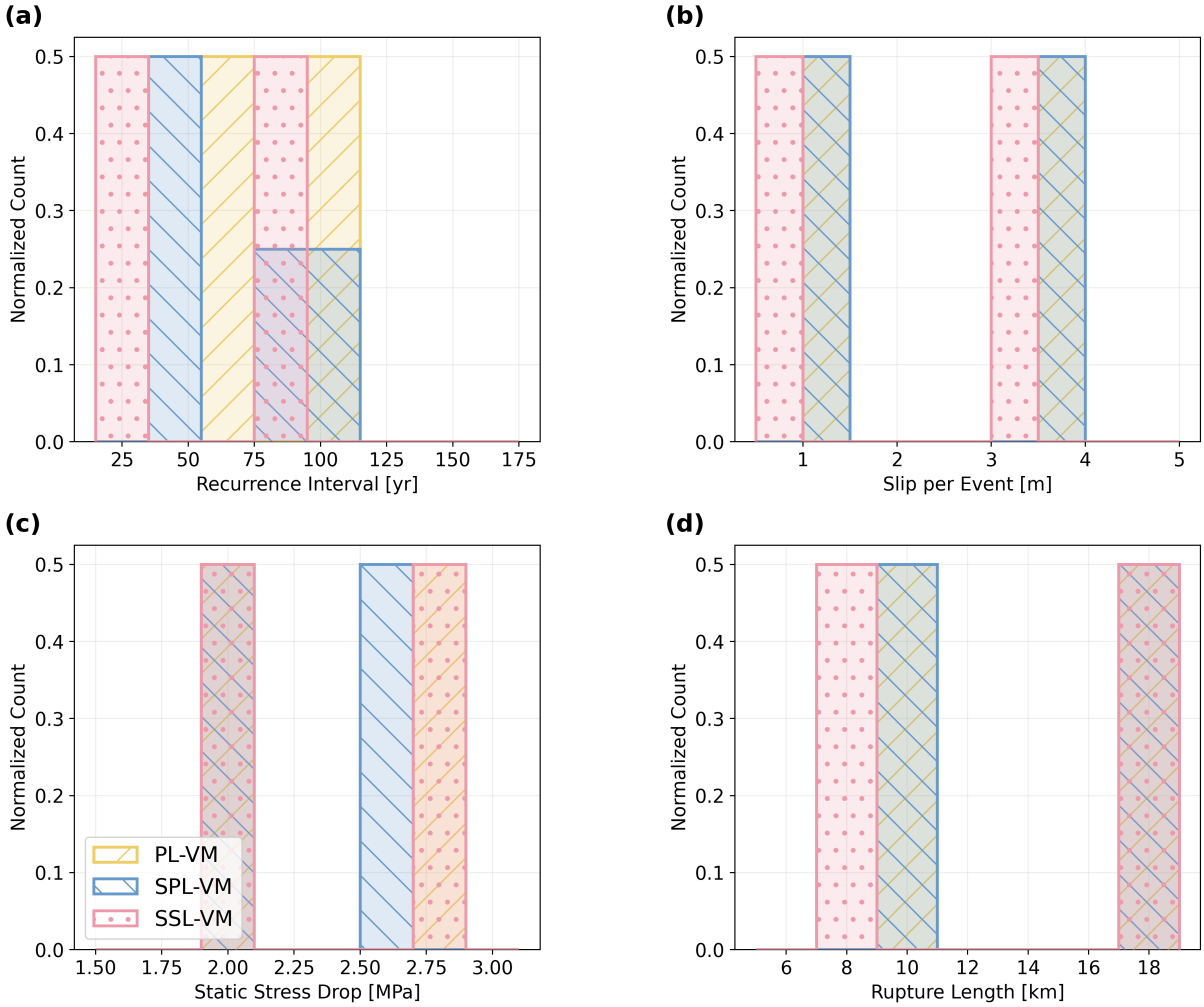

Figure S10. Same as Figure 3 in the main text, but for the models with spatially varying elastic properties (Fig. S2): models PL-VM (yellow, backward hatched), SPL-VM (blue, forward hatched), and SSL-VM (pink).

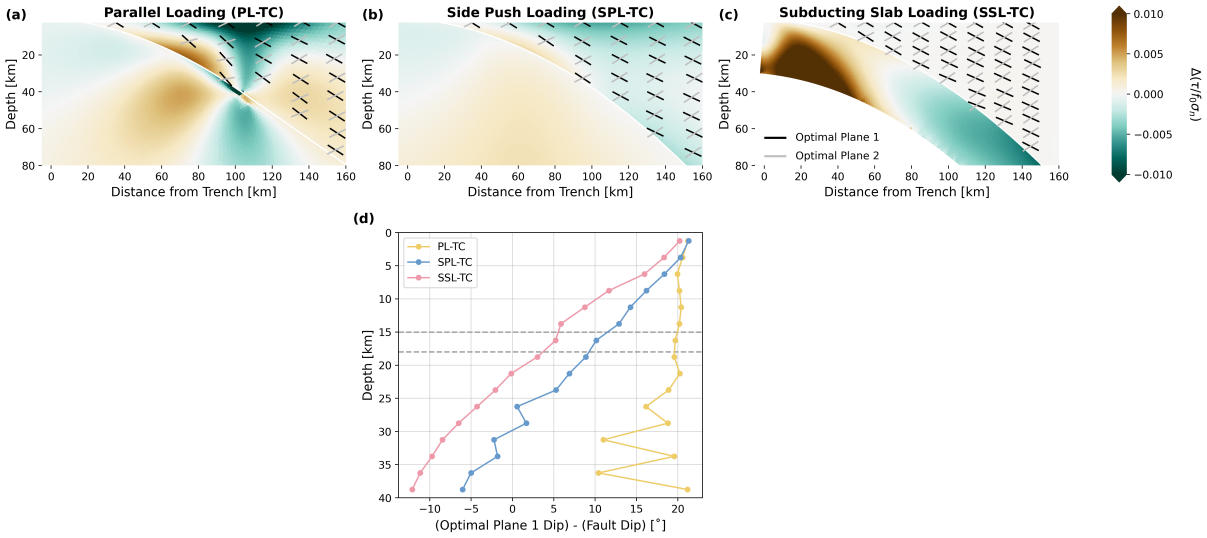

Figure S11. Change in the normalized slip tendency ($\tau/f_0\sigma_n$) resolved on optimally oriented fault planes (black and grey bars) during the last 200 years of simulation in models (a) PL-TC, (b) SPL-TC, and (c) SSL-TC, assuming $f_0 = 0.6$. (d) Difference in dip angle of optimal plane 1 (black bars in panels (a-c)) and fault dip. The two grey dashed lines mark the extent of the seismogenic layer and transition from velocity-weakening to velocity-strengthening rheology.

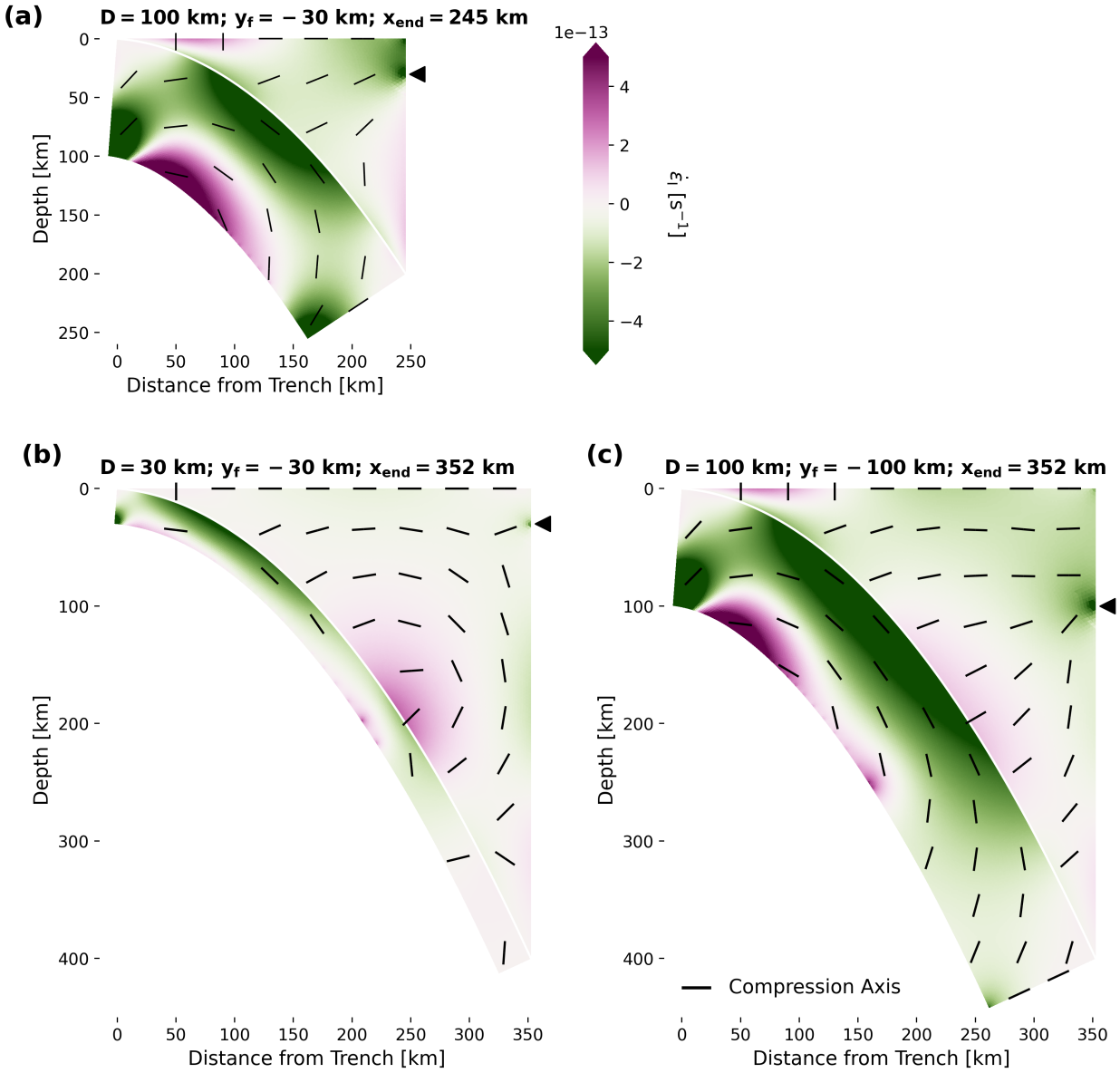

Figure S12. First invariant of strain rate tensors computed from subducting slab loading models with various length scales: models SM1, SM2, and SM3 introduced in Supplementary Text S1. Compare this with Figures 8c and S8b. Color scales are the same as those used in Figure 8 in the main text.

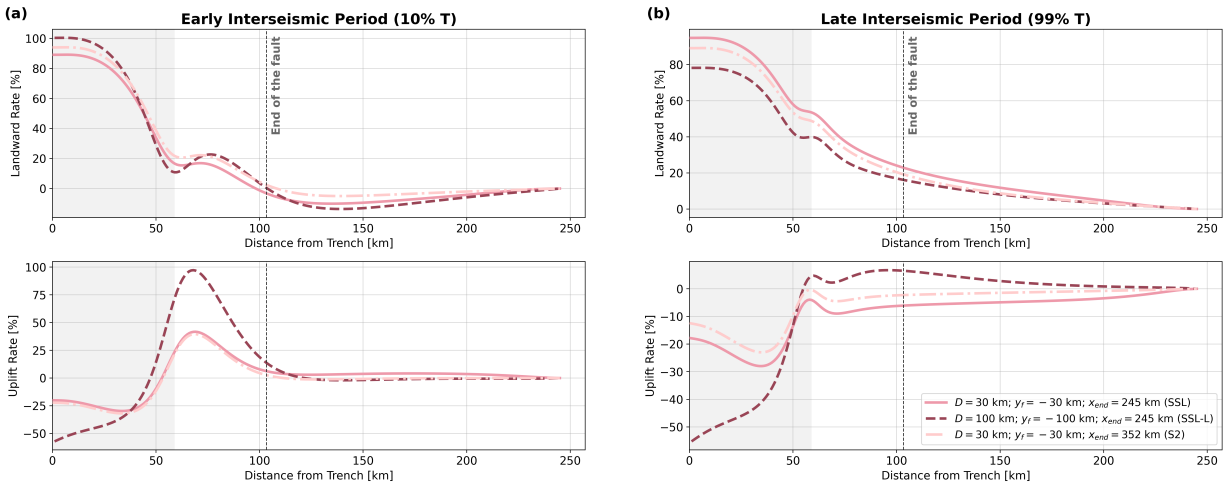

Figure S13. Same as Figure 7 in the main text, but for subducting slab loading models with various length scales: models SM1, SM2, and SM3 introduced in Supplementary Text S1.